

Numerical study of pulsatile flow in a constricted channel

By R. MITTAL¹, S. P. SIMMONS² AND F. NAJJAR³

¹Department of Mechanical and Aerospace Engineering, The George Washington University, Suite T729, 801 22nd St NW, Washington, DC 20052, USA

²Department of Mechanical Engineering, University of Florida, Gainesville, FL 32611, USA

³Center for Simulation of Advanced Rockets, University of Illinois, Urbana-Champaign, IL 61801, USA

(Received 10 October 2001 and in revised form 16 January 2003)

Pulsatile flow in a planar channel with a one-sided semicircular constriction has been simulated using direct numerical simulation and large-eddy simulation. This configuration is intended as a simple model for studying blood flow in a constricted artery. Simulations have been carried out over a range of Reynolds numbers (based on channel height and peak bulk velocity) from 750 to 2000 and a fixed non-dimensional pulsation frequency of 0.024. The results indicate that despite the simplicity of the chosen geometry, the simulated flow exhibits a number of features that have been observed in previous experiments carried out in more realistic configurations. It is found that over the entire Reynolds number range studied here, the flow downstream of the constriction is dominated by the complex dynamics associated with two shear-layers, one of which separates from the lip of the constriction and other from the opposite wall. Computed statistics indicate that for Reynolds numbers higher than about 1000, the flow transitions to turbulence downstream of the region where the separated shear layers first reattach to the channel walls. Large fluctuations in wall pressure and shear stress have also been associated with this reattachment phenomenon. Frequency spectra corresponding to velocity and pressure fluctuations have been analysed in detail and these indicate the presence of a characteristic shear-layer frequency which increases monotonically with Reynolds number. For Reynolds numbers greater than 1000, this frequency is found to be associated with the periodic formation of vortex structures in the shear-layers and the impact of this characteristic shear-layer frequency on the dynamics of the flow is described in detail.

1. Introduction

Atherosclerosis is a disease of the cardiovascular system which involves hardening of arteries due to the deposition of plaque. Localized atherosclerotic constrictions in arteries, known as arterial stenoses, are found predominantly in the internal carotid artery which supplies blood to the brain, the coronary artery which supplies blood to the cardiac muscles, and the femoral artery which supplies blood to the lower limbs. Blockage of more than about 70% (by area) of the artery is considered clinically significant since it presents significant health risks for the patient (Nichols & O'Rourke 1998). Complete closure of the artery can occur if a blood-clot becomes lodged in the stenosis and this can lead to a stroke or a heart attack. In addition to this, moderate as well as severe stenoses can have long-term health consequences. First, the presence of a constriction results in head losses which can reduce the blood

supply through the artery and also impose additional load on the heart. Typically, it is found that these pressure losses are significant only when the internal diameter is reduced beyond about 50% of the nominal value (Young 1979). Secondly, the fluctuations in the blood flow downstream of the stenosis can damage and weaken the internal wall (intima) of the artery. It is accepted that both the wall pressure and shear stress play a role in this. In particular, it has been suggested (Roach 1963; Lighthill 1975) that post-stenotic dilatation (widening of the artery downstream of the stenosis) is due to increased distensibility of the arterial wall induced by high-frequency pressure fluctuations. Furthermore, it has been noted that highly variable wall shear stress in the distal artery can result in a predilection towards atherosclerosis. The variability in wall shear can prevent endothelial cells, which are cells that line the intima, from aligning in the direction of the flow, thereby making the intima more permeable to the entry of harmful blood constituents (Nerem 1992; Giddens, Zarins & Glagov 1993; Zarins & Glagov 1994). Other studies have correlated sites of predilection for atherosclerosis with regions of low shear stress (Friedman *et al.* 1981; Ku *et al.* 1985). Still others have suggested that high shear stress might lead to platelet activation which could accelerate atherosclerosis (Stein, Walburn & Sabbah 1982). The pathological effects on the distal artery are more pronounced for subcritical stenoses (Bomberger, Zarins & Glagov 1981) whereas severe stenoses have actually been found to afford some protection to the distal artery from the formation of atherosclerotic lesions (Creech 1957). In summary, the preceding discussion clearly shows that even though there is some debate in the medical community regarding the relative importance of these various haemodynamic factors, there is little doubt that the fluid dynamics of post-stenotic blood flow plays a crucial role in the progression of atherosclerosis.

Fluid dynamics of post-stenotic flow also plays a key role in the diagnosis of arterial disease. For over two hundred years, it has been known that a stenosed artery produces distinct sounds known as 'arterial murmurs' or *bruits* which can be heard externally (McKusick 1958). Detection of these sounds has gained popularity in the medical community as an inexpensive non-invasive means of screening patients with suspected carotid artery stenoses (Nichols & O'Rourke 1998; Ask *et al.* 1995). The general understanding is that the sounds are produced by the 'disturbed' flow downstream of the stenosis, but until the 1960s little work was done to explore the origin of these sounds. In 1959, Bruns, in a seminal paper, systematically examined possible mechanisms for the generation of these sounds based on the state-of-knowledge at that time. In doing so, he eliminated turbulence, compressibility and cavitation as possible causal mechanisms. Furthermore, by theorizing that the flow downstream of a constriction would be similar to the flow past an obstacle (or a wake flow) and given that vortex shedding in a wake produces the so-called 'Aeolian tones' (Etkin, Korbacher & Keefe 1957) he postulated that arterial murmurs were most probably caused by the periodic shedding of vortices downstream of the constriction. Going a step further, he predicted that with the advent of better techniques for analysing the frequency spectra of these murmurs in the future, it would become possible to extract an accurate picture of the physical conditions that produce this flow.

As predicted by Bruns, a technique called phonoangiography was indeed developed in 1970 (Lees & Dewey 1970) which was designed to predict the severity of the stenotic occlusion in the peripheral arteries through analysis of the sound spectra of the arterial murmurs. The fluid-dynamical basis of this technique was as follows. Sound spectra measured *in vivo* in human subjects with stenosed peripheral arteries were compared with the wall pressure spectra of a fully developed turbulent pipe

flow. Noticing the apparent similarity between the two, it was concluded that the flow downstream of the stenosis was similar to fully developed turbulent pipe flow. Thereafter, using scaling arguments that would be valid for such a flow, it was argued that the break frequency (f_b) in the sound spectrum, i.e. where the spectrum showed a distinct roll-off would scale as d/U where d was the diameter of the stenotic section of the artery and U the volumetric peak flow velocity downstream of the stenosis. Empirical evidence presented in this and subsequent work of Fredberg (1977) and Pitts & Dewey (1979) indicated that $f_b d/U = 1$ was a reasonable estimate of this scaling behaviour. Thus, by measuring f_b and U it would be possible to extract a value for d , the diameter of the stenosed section. It is worth pointing out that this technique ascribed arterial murmurs to turbulence in the post-stenotic flows and did not invoke shear-layer vortex shedding as a cause for these sounds.

Subsequent tests of this technique in clinical settings produced mixed results (Duncan *et al.* 1975). Although there was a positive correlation between the stenotic severity predicted by phonoangiography and that measured independently though a radiographic technique, the relative errors in the prediction were quite high. Furthermore, at the same time, other studies emerged which provided a different view of the dynamics of the post-stenotic flow and the production of arterial murmurs. Of special note here is the study of Tobin & Chang (1976) where wall pressure spectra were obtained at various positions downstream of an axisymmetric stenosis in a pipe with steady inflow. The Reynolds number of the incoming pipe flow ranged from 500 to 4000 which was in line with the Reynolds numbers found in the larger arteries of the human cardiovascular system. Three key observations were made in this study. First, the highest intensity wall pressure fluctuations were produced in the region where the shear layers that separated from the lip of the stenosis attached to the wall of the pipe. Thus, sounds associated with wall pressure fluctuations were due to the shear layer and not the turbulence in the core flow. Secondly, they found that the wall pressure spectra did exhibit a break (or 'corner') frequency beyond which the spectrum rolled off rapidly. However, the break frequency f_b showed a universal scaling of $f_b D/u_j \approx 0.58$ where u_j was the mean jet velocity. Using continuity (i.e. $UD^2 = u_j d^2$), this scaling can be recast as $(f_b d/U) \approx 0.58(D/d)$ and this shows the fundamental difference between this scaling and that of Lees & Dewey (1970). Finally, Tobin & Chang (1976) compared the wall pressure spectrum obtained from their experiments with the same turbulent pipe flow spectrum used by Lees & Dewey (1970) and found significant mismatch in the slope of the spectra beyond the corner frequency.

Jones & Fronek (1987) investigated post-stenotic flows in an axisymmetric geometry with steady inflow over a range of Reynolds numbers (where $Re = UD/\nu$) from 600 to 1500 and suggested $(f_b d/u_j) = Re^{0.72}(d/D)^{0.26}$ as an improved correlation for the break frequency in the pressure spectra. Using continuity, the above expression can be recast as $(f_b d/U) = Re^{0.72}(D/d)^{1.74}$ which can be compared with the corresponding scalings of Lees & Dewey (1970) and Tobin & Chang (1976). Clearly, all three scalings are quite different and this underscores the current lack of consensus and understanding regarding the dynamics of post-stenotic flows. It should also be pointed out that phonoangiography never found widespread use in the medical community owing to its limited predictive capability, and was overcome by duplex scanning ultrasound (Strandness 1994).

Thus, both from the pathological and diagnostic point of view, there is considerable interest in gaining a better insight into the dynamics of post-stenotic flows. Indeed, these two issues have provided the primary impetus for the large number of

experimental studies that have been carried out in the last thirty years. In addition to the references mentioned above, worth noting are the studies of Giddens and coworkers (Giddens, Mabon & Cassanova 1976; Cassanova & Giddens 1978; Ahmed & Giddens 1983, 1984; Lieber & Giddens 1990), Lu *et al.* (1980, 1983), Young and coworkers (Young & Tsai 1979*a, b*; Young 1979) and Clark (1976*a, b*, 1977). In addition, computational modelling is also being used increasingly for the analysis of these flows (Tutty 1992; Tu *et al.* 1992; Taylor & Yamaguchi 1994; Tu & Delville 1996). However, most computations to date have focused on laminar flow regime since computational modelling of such flows in the transitional and turbulent regimes is a challenging proposition. This is because on the one hand, the Reynolds numbers are sometimes high enough that direct numerical simulation (DNS) where all the spatial and temporal scales of turbulence are accurately resolved (Rogallo & Moin 1984) would be extremely taxing on computing resources and on the other hand, both the pulsatile nature of the flow and the relatively low Reynolds number result in a flow that is far from being a fully developed turbulent flow. Consequently, conventional Reynolds-averaged Navier–Stokes (RANS) turbulence models (Wilcox 1998) which are designed primarily for simulating well-developed high-Reynolds-number turbulent flows are not well suited for these arterial flows. Some support for this assertion come from the recent work of Scotti & Piomelli (2001) which clearly indicates the limitations of the predictive capability of existing RANS models for pulsatile flows.

The large-eddy simulation (LES) approach, which lies between DNS and RANS, is a technique well suited for the computational modelling of turbulent arterial flows. Unlike DNS where all the spatial and temporal scales are resolved, in LES, only the energy-containing scales of the turbulence are resolved spatially and temporally and the smaller (subgrid) scales (SGS) are modelled (Rogallo & Moin 1984; Lesieur & Métais 1996). The LES approach has a number of benefits over DNS and RANS. First, since the smallest scales do not need to be resolved, the spatial and temporal resolution required here can be substantially lower than that for a corresponding DNS. Secondly, unlike RANS modelling, LES provides time-accurate information about a wide range of dynamically important scales in the flow. It is therefore capable of providing better physical insight and has the potential of being a more accurate predictive tool. However, the computational expense of these simulations increases rapidly with the Reynolds number and for relatively complex geometries, this has limited the application of LES to only moderately high-Reynolds-number turbulent flows (Piomelli 1999). However, the Reynolds numbers of blood flow in the human cardiovascular system are limited to about $O(10^4)$ and this is well within the reach of present day computers.

The suitability of LES for simulating these moderately high-Reynolds-number cardiovascular flows has been demonstrated in an earlier study (Mittal, Simmons & Udaykumar 2001*a*) where pulsatile flow through a simple geometrical model of a stenosis was simulated at fixed Reynolds and Strouhal numbers using LES and a wide variety of data including mean velocity profiles, higher-order turbulence statistics, wall statistics and frequency spectra extracted from these simulations. In the current study, the same geometrical configuration consisting of a channel with a one-sided semi-circular constriction is employed as a simple model of a stenosed artery and the pulsatile flow through this channel simulated over a wide range of Reynolds numbers using DNS and LES. The focus of the study is on characterization of the spatio-temporal dynamics of the flow in the region downstream of the constriction with special emphasis on those fluid dynamical aspects that are known to play an

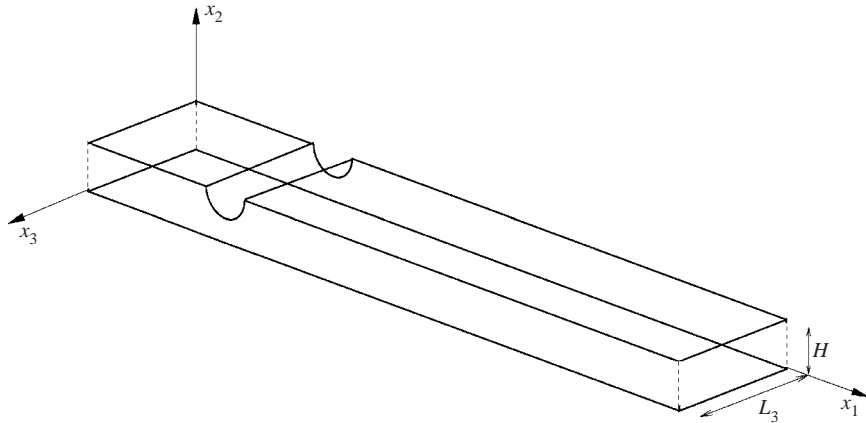


FIGURE 1. Schematic of the channel with semicircular constriction employed in the current study. Note that x_1 , x_2 and x_3 refer to the streamwise, cross-stream and spanwise directions, respectively.

important role in the progression of atherosclerosis and in the non-invasive detection of arterial stenoses.

2. Simulation set-up

2.1. Flow configuration

A relatively simple model of a stenosed artery employed first by Tutty (1992) and subsequently by Mittal *et al.* (2001a) has been chosen for the current study. The geometry is shown in figure 1 and it consists of a planar channel with a one-sided semi-circular constriction on the upper wall centred at $x_1/H = 10$ where H denotes the channel height. However, unlike Tutty who performed a two-dimensional simulation, in the current simulations, allowance is made for periodic variation of flow quantities in the spanwise direction. The diameter of the semicircular constriction is equal to the channel height and therefore, the constriction reduces the channel area by 50%. The channel extends $10H$ and $20H$ upstream and downstream of the centre of the constriction, respectively.

The flow rate per unit channel width (Q) is varied in a sinusoidal manner as $Q(t) = (Q_{max}/2)[1 - \cos(2\pi t/T)]$ where T is the time period of the pulsation and Q_{max} is the maximum flow rate per unit spanwise length of the channel (see figure 2a). The Strouhal number (Ω) which corresponds to the non-dimensional frequency of the inlet flow pulsation is defined as $\Omega = H/T V_{max}$ where $V_{max} = Q_{max}/H$ is the peak inflow bulk velocity. The peak Reynolds number is defined as $Re = V_{max}H/\nu$. Finally, the Womersley number (α) which is used widely in the description of cardiovascular flows (Nichols & O'Rourke 1998) is equal to $(\pi Re \Omega/2)^{1/2}$ for this configuration. It should be pointed out that physiological waveforms are not sinusoidal and there is considerable variation in the waveform depending on the blood vessel under consideration (Nichols & O'Rourke 1998). However, the sinusoidal waveform has been considered a simple prototype of physiological waveforms in a number of past experimental studies (Young & Tsai 1979a, b; Khalifa & Giddens 1981; Ahmed & Giddens 1984) and is also adopted here.

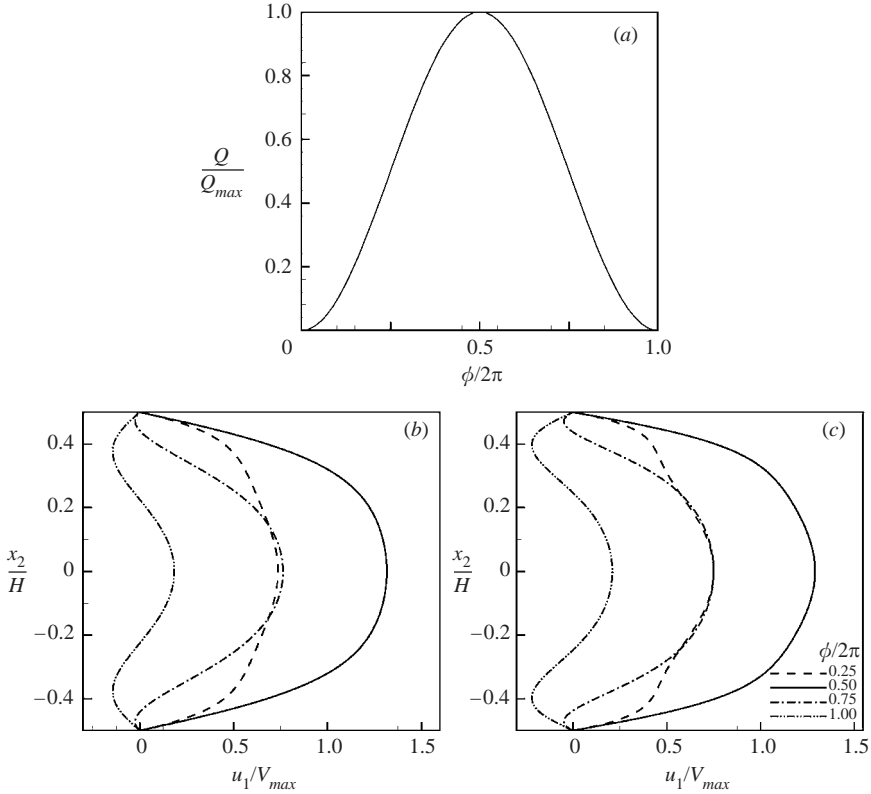


FIGURE 2. Inflow velocity specification based on the Womersley solution (equation (2.2)). (a) Temporal variation of inlet volume flux. (b) Velocity profiles for $\alpha = 6.1$. (c) Velocity profiles for $\alpha = 8.6$.

In our previous computational study (Mittal *et al.* 2001a), a sinusoidally varying parabolic profile was employed at the inlet. However, the pulsatile flow profile in a channel is significantly different from a parabolic profile for Womersley numbers greater than about one (Nichols & O'Rourke 1998). Since the Womersley numbers of interest here are all much greater than one, in the current study the profile corresponding to laminar fully developed pulsatile flow in a channel (Uchida 1956; Loudon & Tordesillas 1998) is employed as the inflow condition. A laminar inflow condition is appropriate for the Reynolds and Womersley numbers employed in the current study (Winter & Nerem 1984). This inflow is obtained as a closed-form solution of the following equation:

$$\rho \frac{\partial u_1}{\partial t} - \mu \frac{\partial^2 u_1}{\partial x_2^2} = -A - B e^{i2\pi t/T}, \quad -\frac{1}{2}H \leq x_2 \leq \frac{1}{2}H,$$

where A and B correspond to the steady and oscillatory pressure gradients and these are chosen so as to give the required minimum and maximum volume fluxes. The final solution to the above equation in non-dimensional form is:

$$\frac{u_1(x_2, t^*)}{V_{max}} = \frac{3}{4} \left[1 - \left(\frac{x_2}{H/2} \right)^2 \right] - i f(\alpha) \left[1 - \frac{\cosh(2\alpha \sqrt{i} x_2)}{\cosh(\alpha \sqrt{i} H)} \right] e^{i2\pi \Omega t^*},$$

and the real part of this solution is used as the inlet velocity condition. In the above equation, $f(\alpha)$ is a known function of α which appears as a consequence of matching the volume flux conditions (Simmons 2001) and $t^* = tV_{max}/H$ is the non-dimensional time. Note that the shape of the inlet velocity profile depends only on the Womersley number and the profile shapes for $\alpha = 6.1$ and 8.6 are shown in figure 2 for four different phases in the pulsation. For the current configuration, these correspond to $Re = 1000$ and 2000 , respectively. Note that the phase, ϕ , is defined as $2\pi t/T$. At the exit, a convective boundary condition (Kaltenbach *et al.* 1999) is applied and this allows the vortex structures to exit the domain with minimal reflections.

The spanwise domain size (L_3) is chosen to be equal to $3H$ and periodic boundary conditions applied on the spanwise boundaries. These boundary conditions are intended to model the spanwise homogeneous flow that would be present in a channel with an infinite spanwise extent. As such it is imperative to demonstrate that the computed flow is independent of the choice of the spanwise domain size and this issue is addressed later in the paper.

The initial condition in the channel corresponds to the inflow velocity profile where the streamwise velocity is scaled appropriately at every streamwise station so as to satisfy local mass conservation. Furthermore, a small disturbance which is random in time and spanwise direction is imposed on all the components of velocity at the inflow at the beginning of the simulation for ten time steps. Subsequently, the three-dimensionality is allowed to develop on its own through the inherent instability of the flow. Eventually, the flow reaches a statistically stationary state and the simulations are carried beyond this for about eight cycles for all cases. All statistics as well as other data such as temporal variations and frequency spectra presented in this paper are over this time period of about eight cycles. The simulations have been carried out on a 195 MHz SGI Origin-2000 multiprocessor computer. The solver has been parallelized using OpenMP (Chandra *et al.* 2000) and up to eight nodes have been used for these simulations. Each cycle takes about 120 CPU hours on one node and a typical simulation takes about 1500 CPU hours on one node of this computer.

The flow downstream of an arterial stenosis is characterized by separating transitioning shear layers that evolve under the influence of a pulsatile inflow and interact with the arterial walls downstream of the stenosis. The planar geometric model that has been chosen here is relatively simple and obviously does not account for the circular cross-section of a typical artery. However, it does include the important geometrical features of an arterial stenosis mentioned above and preliminary computations (Mittal *et al.* 2001a) indicate that the flow in this simple configuration exhibits many of the key features (as mentioned above) that characterize post-stenotic flow in a realistic artery. The simplicity of the chosen geometry reduces the computational expense and allows us to perform a comprehensive computational study and obtain insight into the physics of this flow. We expect that this will set the stage for computational studies of a more realistic geometrical configuration in the future.

2.2. Numerical methodology

The code is based on a hybrid second-order finite-difference/spectral method which solves the three-dimensional incompressible Navier–Stokes equations in primitive variables (velocity and pressure) in generalized coordinates on a spanwise periodic domain. It has been well established that blood flow in the larger vessels can be modelled quite accurately as a Newtonian fluid (Pedley 1980; Fung 1997) and this justifies the use of the Navier–Stokes equations. Figure 3 shows a two-dimensional

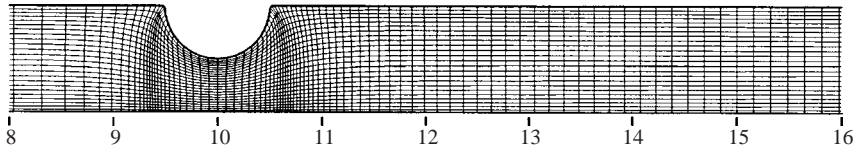


FIGURE 3. Two-dimensional view of the mesh used in case 1. Only every third mesh point in each direction is shown.

view of a typical curvilinear grid used in the current simulation. A second-order central difference is used in the streamwise and wall-normal directions whereas Fourier collocation is used in the spanwise direction. A staggered-mesh is used in the plane of the generalized coordinates with volume fluxes, i.e. contravariant velocity vector components weighted with the Jacobian as dependent variables (Orlandi 1989; Rosenfeld, Kwak & Vinokur 1991; Choi, Moin & Kim 1992). The spanwise velocity component is collocated at the pressure nodes and phase-shifting dealiasing (Rogallo 1981) is performed in the spanwise direction in order to stabilize the computations and enhance accuracy. Regarding the choice of the spatial discretization scheme, it has been demonstrated (Mittal & Moin 1997) that numerical dissipation can overwhelm the contribution of the SGS model and, therefore, dissipative numerical schemes are not well suited for LES. The spatial discretization scheme employed in the current computations has been constructed to ensure conservation of kinetic energy (Ferziger & Peric 1999) which allows for a stable computation without the need for numerical dissipation.

The incompressibility constraint is enforced with a time-split (Chorin 1968) technique which is second-order accurate in time (Choi *et al.* 1992). A mixed explicit–implicit scheme is used for the momentum equation where the viscous terms in the wall normal direction are integrated by means of the Crank–Nicholson method and all other terms are integrated with a low-storage third-order Runge–Kutta scheme (Spalart, Moser & Rogers 1991). By taking a Fourier transform in the spanwise direction, the pressure Poisson equation is reduced to a series of two-dimensional Helmholtz equations, one for each spanwise wavenumber. Each of these equations is then solved with a multigrid technique. The average time step (Δt) used in these simulations is about $5 \times 10^{-4}T$.

The subgrid-scale model used to account for the effect of the unresolved turbulent motions, is a version of the dynamic model (Germano *et al.* 1991) suitable for generalized coordinates. A least-squares contraction (Lilly 1992) is used to compute the SGS model coefficient which is obtained as a spanwise averaged quantity. The test filter is applied in the streamwise and spanwise directions using the trapezoidal rule to approximate the filter, and the test-to-grid filter ratio is $\tilde{\Delta}/\Delta = \sqrt{6}$. The present numerical method and the associated solver have been tested extensively in several laminar and turbulent flows (Mittal & Moin 1997; Kaltenbach *et al.* 1999; Mittal *et al.* 2001a, b) and further details regarding the method can be found in these papers.

A priori, there is nothing in the dynamic SGS modelling procedure that would limit its use in pulsatile flows. In fact, the dynamic model has been used successfully in LES of a bluff-body wake flow (Mittal & Moin 1997) where the flow in the near wake can be viewed as ‘pulsatile’ in that it oscillates in time with a dominant frequency and even reverses direction during this pulsation. The fact that in the current case, the pulsation is explicitly imposed as opposed to being produced naturally by von Kármán vortex

shedding (in the case of the wake) is of no consequence to the procedure. As will be shown in § 3.1, the dynamic modelling procedure produces SGS eddy viscosity which, in its magnitude and variation, is in line with the observed physics of the flow.

2.3. Data reduction

It is also useful at the outset to define the various averaging operations employed in the current study. For a generic flow variable g , the mean over M cycles is computed as

$$\langle g \rangle(x_1, x_2) = \frac{1}{L_3} \frac{1}{MT} \int_{t_0}^{t_0+MT} \int_0^{L_3} g(x_1, x_2, x_3, t) dx_3 dt,$$

where t_0 corresponds to the beginning time of the averaging process. Deviation from this average is computed as

$$g' = g - \langle g \rangle.$$

In addition, for a pulsatile flow it is useful to compute a phase average (Reynolds & Hussain 1972; Lieber & Giddens 1990). The phase average over M cycles is computed as

$$\tilde{g}(x_1, x_2, t) = \frac{1}{L_3} \frac{1}{M} \sum_{n=0}^{M-1} \int_0^{L_3} g(x_1, x_2, x_3, t + nT) dx_3.$$

Deviation from this phase average is computed as

$$g'' = g - \tilde{g}.$$

The phase average \tilde{g} represents the time-varying coherent (or deterministic) part of the flow and primarily contains time scales directly associated with the pulsation. The deviation from the phase average (g'') represents the non-deterministic motions and therefore this decomposition provides a means of separating scales that are associated with the pulsation from those associated with turbulence. In this paper, these fluctuations are referred to as ‘turbulent’ fluctuations. Finally, the instantaneous spanwise average of a variable g is defined as

$$\langle g \rangle_3(x_1, x_2, t) = \frac{1}{L_3} \int_0^{L_3} g(x_1, x_2, x_3, t) dx_3.$$

3. Results and discussion

Table 1 gives a summary description of the various simulations that are reported in the current study. Reynolds numbers range from 750 to 2000 and the Strouhal number of the pulsation is fixed at 0.024. Thus, the Womersley number in the current study varies from 5.3 to 8.6 and this range of parameters is consistent with the values typical for blood flow in the larger arteries of the human cardiovascular system (Pedley 1980; Fung 1997; Nichols & O’Rourke 1998). All computations for which detailed results are reported in this section have been performed on a $320 \times 64 \times 32$ ($N_{\xi_1} \times N_{\xi_2} \times N_{x_3}$) mesh, where ξ_1 refers to the family of grid lines that run from the inlet to the exit, ξ_2 corresponds to those that run between the top and bottom walls, and x_3 refers to the spanwise grid lines. Furthermore, as mentioned earlier, the spanwise domain size has been chosen equal to $3H$. The rationale used in adopting these computational parameters was as follows. First, earlier computations of this flow (Mittal *et al.* 2001a) for $Re = 2000$ were used to guide the initial design of the $320 \times 64 \times 32$ mesh. As is clear from figure 3, enhanced wall normal resolution is provided to the flow in the vicinity of the two walls. In addition, the region immediately downstream of the

Case number	Re	Solver	L_3/H	N_{ξ_1}	N_{ξ_2}	N_{x_3}	α	S
1	2000	LES	3	320	64	32	8.6	1.80
2	2000	LES	3	320	96	32	8.6	–
3	2000	LES	5	320	64	32	8.6	–
4	1700	LES	3	320	64	32	8.0	1.72
5	1400	DNS	3	320	64	32	7.3	1.63
6	1000	DNS	3	320	64	32	6.1	1.55
7	750	DNS	3	320	64	32	5.3	1.20

TABLE 1. Various simulations reported in the current study. For all simulations $\Omega = 0.024$ and $(h/H) = 0.5$. Furthermore, N_{ξ_1} , N_{ξ_2} and N_{x_3} denote the number of cells in streamwise, wall-normal and spanwise directions, respectively. Also shown in the last column are the observed values of (S) corresponding to the dominant non-dimensional shear-layer vortex-formation frequency for the various cases. Further discussion regarding this quantity can be found in § 4.4.

constriction has relatively fine streamwise grid spacing. The key issue in choosing a mesh for the current simulations is to provide adequate resolution for the thin shear layer that is expected to separate from the lip of the constriction. The topology of the structured grid employed here is such that it is not easy to increase the ξ_2 grid spacing selectively in this region. The only way to increase the local resolution is, in fact, to increase the total number of grid points. Thus, a relatively fine mesh with 64 grid points in the ξ_2 -direction was chosen and this resulted in over 12 grid points across the width of the shear layer for the $Re = 2000$ case.

It is useful to point out that in a previous LES study of flow through a planar diffuser (Kaltenbach *et al.* 1999) which employed the same code, a grid with 64 grid points across the channel width was successfully used for simulating flow at a Reynolds number (based on channel width and bulk flow velocity) of about 9000. In the current study, the Reynolds number is substantially lower and thus 64 points should provide more than adequate resolution. However, despite the seeming adequacy of this resolution, it was thought necessary to check the sensitivity of the computed results to the resolution in the ξ_2 -direction. At the outset, however, it should be pointed out that grid dependence for large-eddy simulations has to be viewed from a slightly different perspective from DNS or computations of laminar flows. Since in the current LES methodology, the range of resolved scales is determined by the grid resolution, it is expected that the computed flow will show some dependence on the mesh resolution. This dependence will be apparent until the resolution becomes fine enough that the LES starts to qualify as a DNS, i.e. the grid cutoff extends well into the dissipation range. Thus, strict grid independence of the computed solution is not expected in an LES. Instead, it is adequate to demonstrate that the primary flow features such as mean velocity and fluctuation intensity do not vary significantly with the grid. This is the viewpoint taken in the current study.

Thus, in order to check the sensitivity of the flow to the ξ_2 -resolution, the $Re = 2000$ LES simulation (Case 1) was repeated on a $320 \times 96 \times 32$ mesh (Case 2) which has 50% more mesh points in the ξ_2 -direction than the previous mesh. Figure 4(a) shows a comparison of the mean streamwise velocity profiles and it can be observed that the two sets of velocity profiles are in very good agreement with each other. In addition to this, we have also compared the fluctuation kinetic energy $\langle u'_i u'_i \rangle / 2$ profiles for the two cases and these also compare favourably for the two simulations. Based on these

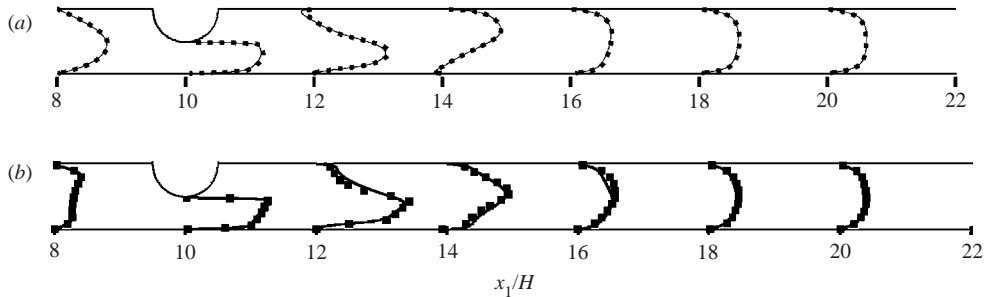


FIGURE 4. Comparison of flow statistics for cases 1 and 2 ($Re = 2000$) which have different wall-normal grid resolutions. Solid line, case 1; symbols, case 2. (a) Mean streamwise velocity $\langle u_1 \rangle$ profiles. In these profile plots, unit velocity corresponds to a distance of $0.2H$ in the streamwise direction. (b) Profiles of fluctuation kinetic energy $\langle u'_i u'_i \rangle / 2$. In these profile plots, a distance of H in the streamwise direction corresponds to an energy level of 0.25.

results, the $320 \times 64 \times 32$ mesh was deemed adequate for LES at $Re = 2000$. The same mesh was then employed for all the other lower Reynolds-number simulations with the implicit understanding that a mesh adequate for $Re = 2000$ would be more than adequate at lower Reynolds numbers. However, it was found that for the $Re = 1400$ simulation, the contribution of the SGS model was quite small and ‘turning off’ the SGS model did not have any noticeable impact on the flow. This indicated that for the lower Reynolds numbers, the mesh resolution was high enough for the computation to qualify as a DNS and the SGS model was then turned off for all the lower Reynolds-number simulations. Since the dynamic SGS model adds about a 10% overhead to the CPU time in the current simulations, turning off the model speeds up the solution process.

As mentioned earlier, it is important in such flows to establish that the computed results do not depend on the spanwise domain size employed in the simulations (Mittal & Balachandar 1997; Kaltenbach *et al.* 1999). In our previous computations (Mittal *et al.* 2001a) a spanwise domain size of H was employed and this was subsequently found not to be large enough to eliminate domain size effects. In the current simulations, a larger spanwise domain size of $3H$ is chosen in order to remedy the situation. However, despite the threefold increase in the domain size, it was still thought prudent to demonstrate conclusively, the adequacy of this domain size. In order to accomplish this, the $Re = 2000$ simulation (Case 1) has been repeated with a domain size of $L_3 = 5H$. However, maintaining the same spanwise grid resolution as Case 1 on this larger domain would have required about 54 grid points and this would have resulted in a proportional increase in the computational expense. In order to avoid this, the spanwise mesh size of 32 mesh was retained and this resulted in a simultaneous decrease in the spanwise resolution for this simulation. Thus, comparison of the flow computed for these two cases serves to demonstrate not only the insensitivity of the flow to the spanwise domain size but also to the spanwise resolution. Figure 5 shows a comparison of the mean streamwise velocity profiles for these two simulations and it can be seen that the mean flow downstream of the constriction does not change significantly with the spanwise domain size. In order to further demonstrate the adequacy of the spanwise domain size and resolution, we have also compared the spanwise normal stress $\langle u_3^2 \rangle$ for Cases 1 and 3 in figure 5(b). The magnitude and variation of this quantity is most sensitive to the three-dimensional

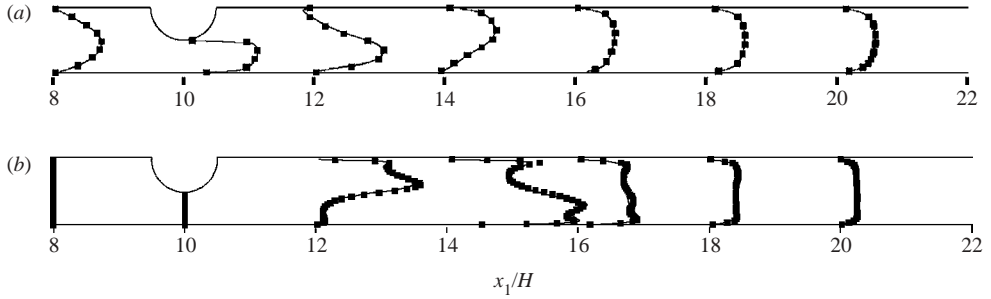


FIGURE 5. Comparison of flow statistics, for cases 1 and 3 ($Re = 2000$) which have spanwise domain sizes of $3H$ and $5H$, respectively. Solid line, case 1; symbols, case 3. (a) Comparison of mean streamwise velocity $\langle u_1 \rangle$. In these profile plots, unit velocity corresponds to a distance of $0.2H$ in the streamwise direction. (b) Comparison of spanwise normal stress $\langle u_3^2 \rangle$. In these profile plots, a distance of H in the streamwise direction corresponds to a stress value of 0.022 .

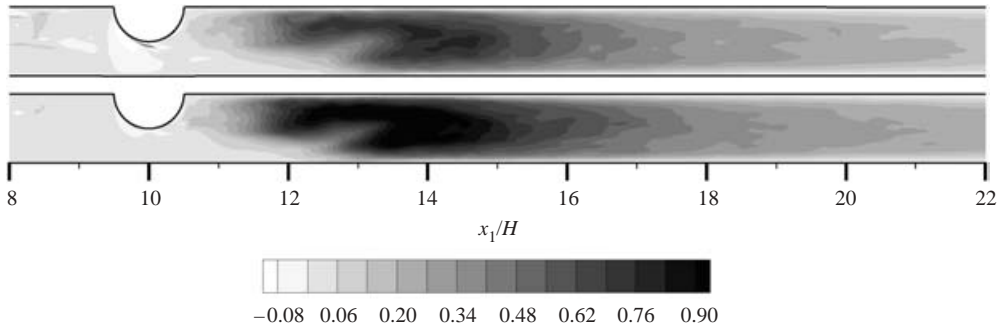


FIGURE 6. Mean normalized SGS eddy viscosity $\langle \nu_t / \nu_m \rangle$ (a) $Re = 1700$, (b) 2000 .

vortex structures formed in the flow and it is, therefore, a good diagnostic tool for checking the sensitivity of the computed results to the spanwise domain size and grid resolution. As can be seen in the figure, despite the significant increase in domain size and accompanying decrease in the grid resolution, the stress profiles for the two cases compare well, thereby further confirming the adequacy of the spanwise domain size and resolution.

Thus, a spanwise domain size of $3H$ is found to be sufficient for the current computations and we have therefore chosen to use this domain size for all subsequent simulations. Also, since 32 grid points in the span was found to be sufficient for $Re = 2000$, it was assumed that it would be more than adequate at the lower Reynolds numbers.

3.1. Role of SGS model

Although the focus of this paper is on the flow physics, it is nevertheless useful to provide some information on the role that the SGS model plays in the large-eddy simulations reported in this study. Figure 6 shows contour plots of the mean SGS eddy viscosity $\langle \nu_t \rangle$ normalized by the molecular viscosity ν_m , for $Re = 2000$ (Case 1) and $Re = 1700$ (Case 4). First, for both of these simulations, the region of significant SGS eddy viscosity is downstream of the constriction where, as will be shown in subsequent sections, the flow transitions to turbulence. Thus, the dynamic

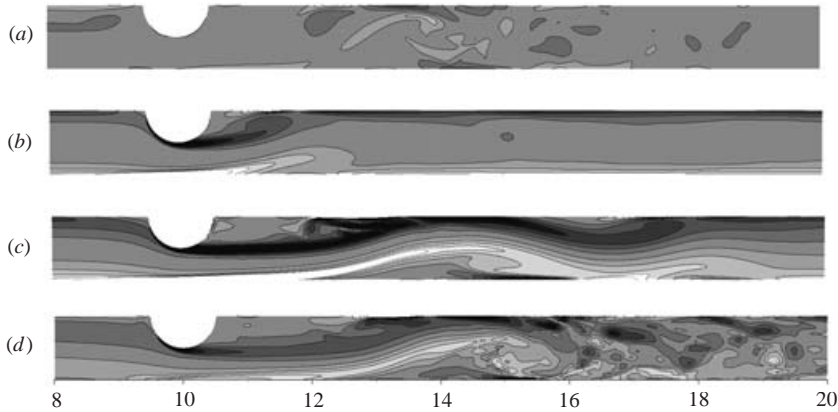


FIGURE 7. Sequence of contour plots of spanwise-averaged spanwise vorticity non-dimensionalized by V_{max}/H plots at four phases in the pulsation for $Re = 750$. Eight equispaced contour levels from -7.78 to $+7.78$ are shown. The phase ϕ has been set to zero at the beginning of the pulsation when the flow rate is zero. (a) $\phi = 0$, (b) $\phi = \pi/2$, (c) $\phi = \pi$, (d) $\phi = 3\pi/4$.

SGS model correctly introduces dissipation primarily in regions where there are significant turbulent fluctuations and almost no dissipation in regions where the flow is unsteady but laminar. This is one of the features of the dynamic SGS model that makes it suitable for computing such flows.

For $Re = 2000$, the peak eddy viscosity is about 0.97 implying that the model adds up to 97% extra dissipation into the flow. As the Reynolds number is reduced to 1700 while keeping the same grid, the peak SGS eddy viscosity reduces to about 0.75 which is consistent with expectation of reduced energy in the SGS scales at the lower Reynolds numbers. For $Re = 1400$, it was found that the SGS eddy viscosity reduced significantly and turning off the SGS model did not have any significant effect on the computed results. This implied that the $320 \times 64 \times 32$ mesh was fine enough to capture all significant scales of the flow at $Re = 1400$. Thereafter, in order to reduce the CPU time, the SGS model was turned off for all simulations with Reynolds number less than or equal to 1400 and these computations are considered to be well-resolved direct numerical simulations.

4. Flow physics

With the numerical aspects of the study described and the accuracy and fidelity of the simulations firmly established, we now focus on the analysis of the simulation results for the various cases. In the following sections, we will describe the results of Cases 1 and 4–7. As pointed out earlier, all results presented here are for the statistically stationary flow regime and statistics have been accumulated over at least eight flow cycles for all cases.

4.1. Vortex dynamics

Figures 7, 8 and 9 show sequences of spanwise-averaged spanwise vorticity contours (denoted by $\langle \omega_3 \rangle_3$) for $Re = 750$, 1400 and 2000, respectively. Each sequence consists of four plots which correspond to phase $\phi = 0, \pi/2, \pi$ and $3\pi/4$, respectively, where the phases have been arbitrarily set to zero at the beginning of the cycle where the flow rate is zero. In terms of the flow pulsation, these phases correspond to zero mean

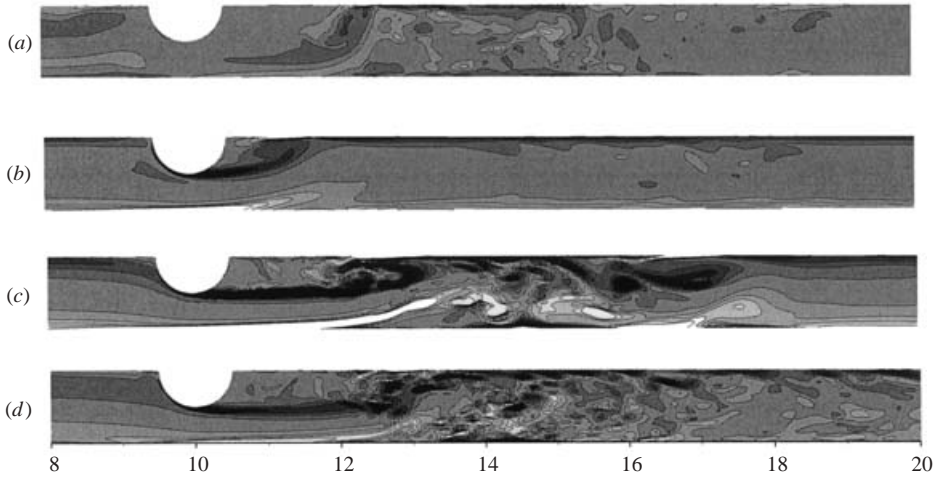


FIGURE 8. Sequence of spanwise-averaged spanwise vorticity plots at four phases in the pulsation for $Re = 1400$. Contour levels are the same as in previous figure. (a) $\phi = 0$, (b) $\phi = \pi/2$, (c) $\phi = \pi$, (d) $\phi = 3\pi/4$.

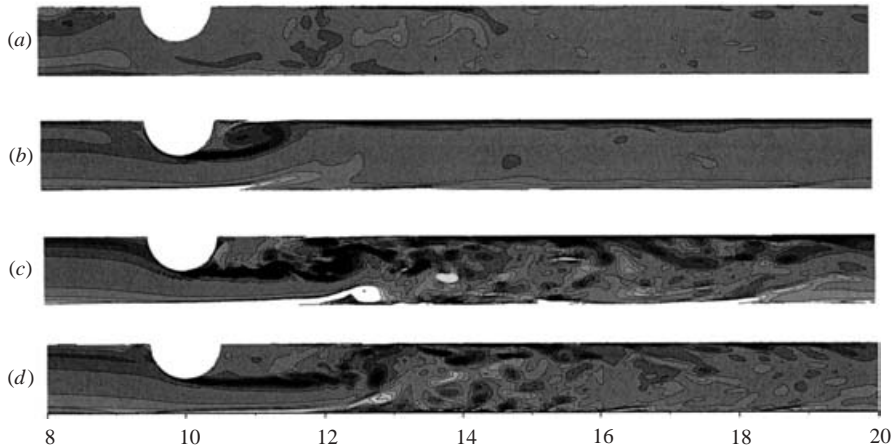


FIGURE 9. Sequence of spanwise-averaged spanwise vorticity plots at four phases in the pulsation for $Re = 2000$. Contour levels are the same as in previous figure. (a) $\phi = 0$, (b) $\phi = \pi/2$, (c) $\phi = \pi$, (d) $\phi = 3\pi/4$.

flow, maximum acceleration, maximum flow and maximum deceleration. The same contour levels are used in all these plots so as to facilitate direct comparison between them.

Figure 7, which corresponds to $Re = 750$, the lowest Reynolds-number case simulated in the current study, shows a sequence of four plots of the spanwise-averaged spanwise vorticity. Figure 7(a) corresponds to the phase in the cycle where the mean inlet flow rate is zero and the spanwise vorticity contours show the remnants of the vortical structures formed downstream of the stenosis in the previous cycle. Figure 7(b) corresponds to the phase in the pulsation where the flow rate is half its maximum value and the flow has maximum acceleration. It can be seen from

the figure that the rapidly increasing velocity results in the creation of a shear layer at the lip of the constriction. This shear layer separates and begins to roll up into a counterclockwise rotating vortex which is observed to attach to the upper wall at about $x_1/H = 11.5$. Furthermore, the increasing velocity in the stenosis region induces a relatively intense vorticity layer on the bottom wall which is also observed to separate and lift up from the bottom wall. The separation location coincides roughly with the location where the upper shear layer attaches to the upper wall and this is due to the fact that the effective area available for the flow coming through the constriction begins to increase only when the upper shear layer rolls upwards. This increase in the effective area creates an adverse pressure gradient which induces the separation of the vorticity layer on the lower wall.

Figure 7(c) corresponds to the phase of maximum flow rate through the channel and the vorticity plot indicates a relatively well-ordered laminar flow. Furthermore, as the lower separated shear layer rolls up into a large vortex at about $x_1/H = 15$, it reattaches on the lower wall. This leads to an expansion in the effective area for the flow above this shear layer and the resulting adverse pressure gradient induces the separation of the upper shear at about $x_1/H = 16$. Further downstream, the separated upper shear layer attaches for the second time at about $x_1/H = 17$ and this again induces the separation of the lower shear layer, an event that occurs at about $x_1/H = 18$. This behaviour of alternate separation and reattachment in the two shear layers has been well documented by Tutty (1992) who studied the same flow at a lower Reynolds number using two-dimensional simulations.

Figure 7(d) corresponds to the phase where the flow rate is half its maximum value and the mean flow has maximum deceleration. The flow still looks well ordered and laminar up to about $x_1/H = 14$ where the lower vorticity layer rolls up into a large clockwise vortex with an identifiable vortex core at about $x_1/H = 15$. However, further downstream, the shear layers break up into a complex array of vortex structures. The spatio-temporal dynamics of this region will be explored further in subsequent sections.

Figure 8 shows the corresponding sequence of vorticity plots for $Re = 1400$ which is roughly in the middle of the Reynolds-number range studied here. The vortex dynamics in the first two phases is quite similar to that observed at the lower Reynolds number. Significant differences begin to emerge in figure 8(c) which corresponds to the maximum flow rate. In particular, the vortex that rolls up in the lower separated shear layer begins to disintegrate into a complex system of distinct smaller vortices. Further downstream, the flow is relatively more well ordered and some remnants of the alternate separation/reattachment structure are still visible. The upper shear layer which separated from the lip of the constriction also shows some breakup into discrete vortices which is visible between x_1/H of 12 and 13. The flow in the next phase shown in figure 8(d) is significantly different from that at the lower Reynolds number. The vortex formed in the lower shear layer has completely disintegrated into smaller scale structures and no vortex core is identifiable. The breakup of the upper shear layer into smaller scale structures is also observed to be in an advanced stage.

The final sequence of plots in figure 9 is for $Re = 2000$ which is the highest Reynolds number simulated here. Again it is found that the flow up to the first two stages is quite similar to that at the lower Reynolds numbers. However, in the next phase (figure 9c), the flow is completely different from that observed for the previous two cases. First, the shear layer on the lower wall, which for the lower Reynolds numbers was observed to lift up to and beyond the channel centreline at around $x_1/H = 14$, is found not to exhibit such behaviour at $Re = 2000$. Instead, the lower

shear layer separates at about $x_1/H = 12$ and immediately rolls up into a series of compact vortices in the vicinity of the lower wall. Furthermore, the upper shear layer that separated from the lip of the constriction rolls up into distinct Kelvin–Helmholtz type rollers observed in a canonical shear layer (Brown & Roshko 1974). Downstream of about $x_1/H = 13$, the vortex structures from the two separated boundary layers interact to produce a highly complex flow. In the last phase (figure 9d) the deceleration of the flow is observed to diminish the strength of the vortex structures. In particular, neither of the two separated boundary layers are observed to roll up into distinct vortices.

Although to our knowledge, the formation of such vortex structures has not been observed before in any previous computational studies of such flows (barring the earlier work of Mittal *et al.* 2001a), the presence of these structures in post-stenotic flows is well established. In a seminal study exploring the origin of ‘murmurs’ in the cardiovascular system, Bruns (1959) effectively eliminated turbulence, compressibility and cavitation as possible causes and convincingly argued that these sounds were most probably the result of the periodic formation of compact vortex structures in the flow downstream of arterial constrictions. Since then, a number of experimental studies have observed and described the formation of such vortex structures in the flow downstream of a constriction. Of particular note in this regard are the studies of Cassanova & Giddens (1978) and Lu *et al.* (1983). In the former, dye visualizations and hot-film anemometric measurements of the velocity were made in the flow downstream of a constriction in a pipe. Both steady and pulsatile flows were employed and the Reynolds numbers (based on pipe diameter and inlet velocity) ranged from about 300 to 2500. Flow visualizations clearly indicated the presence of vortex shedding in the separated shear layers and frequency spectra exhibited a distinct peak corresponding to this vortex shedding. In the study of Lu *et al.* (1983), the flow downstream of an axisymmetric constriction in a pipe was measured using laser-Doppler anemometry. The inlet flow to the pipe was steady and the Reynolds number (based on constriction diameter and velocity through the constriction) was about 50 000. The frequency spectra of the velocity exhibited a distinct peak which was associated with the periodic formation of vortex structures in the separated shear layers. In addition to these two studies, the vortex-shedding phenomenon in post-stenotic flows has also been described in other studies by Giddens and coworkers (Khalifa & Giddens 1981; Ahmed & Giddens 1983, 1984; Lieber & Giddens 1990).

It should be pointed out that all the flow visualizations shown using spanwise-averaged data do not give a full appreciation of the three-dimensionality of the flow. Figure 10 shows a three-dimensional visualization of the instantaneous spanwise vorticity at a phase corresponding to figure 9(c). From this figure, becomes clear that the shear layers that develop on the constriction and on the lower wall are almost perfectly two-dimensional but become highly three-dimensional further downstream.

4.2. Mean flow characteristics

Figure 11 shows the streamlines corresponding to the mean velocity for the $Re = 750, 1400$ and 2000 cases simulated here and a few trends are readily apparent from this figure. For all cases, a relatively large recirculation region is found to exist downstream of the constriction in the time-mean flow. These recirculation zones are indicative of regions where the flow is reversed over a significant portion of each cycle. Thus, appearance of these recirculation regions is of pathological significance since first, these are regions of low shear and secondly, these regions can increase the residence time of blood constituents which can eventually pass into the arterial

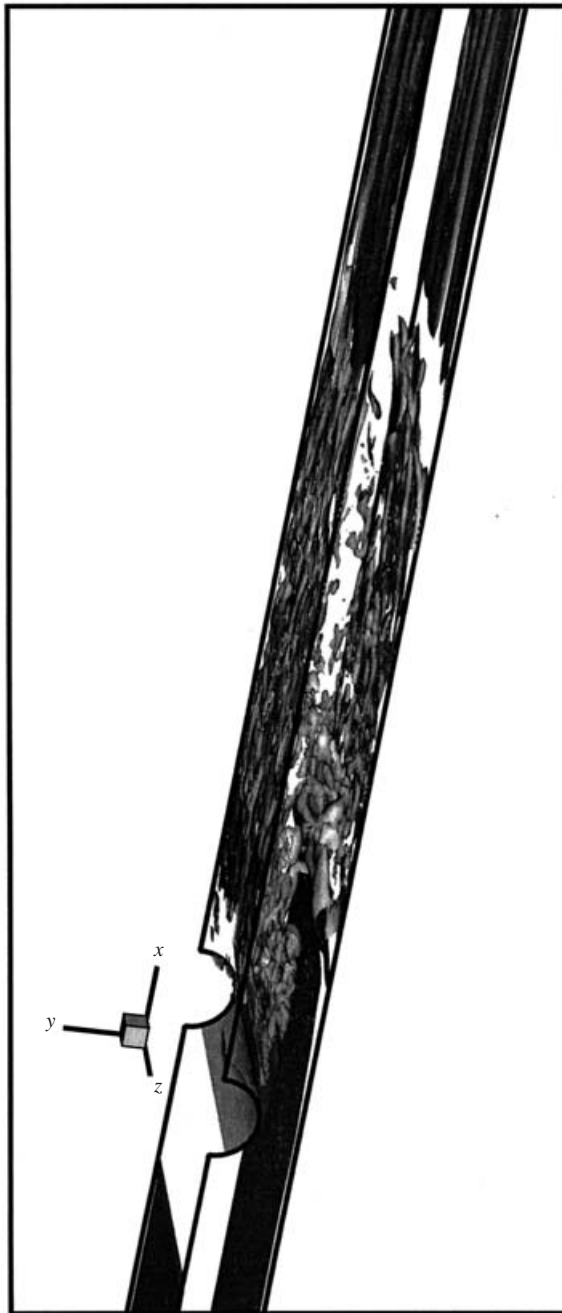


FIGURE 10. Isosurfaces of instantaneous spanwise vorticity for $Re = 2000$ corresponding to figure 9(c). Two isofurfaces corresponding to vorticity levels of ± 7.8 have been plotted.

wall (Friedman *et al.* 1981). The downstream extent of the recirculation zone has been determined by examining the mean wall shear and noting the location where this quantity changes sign. For $Re = 750$, this region extends over a length of about $3.5H$ from the tip of the constriction. This length decreases with increasing

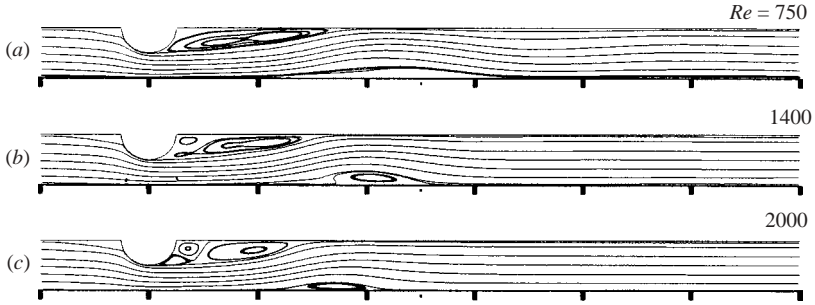


FIGURE 11. Streamline plot corresponding to mean velocity (a) $Re = 750$, (b) $Re = 1400$, (c) $Re = 2000$.

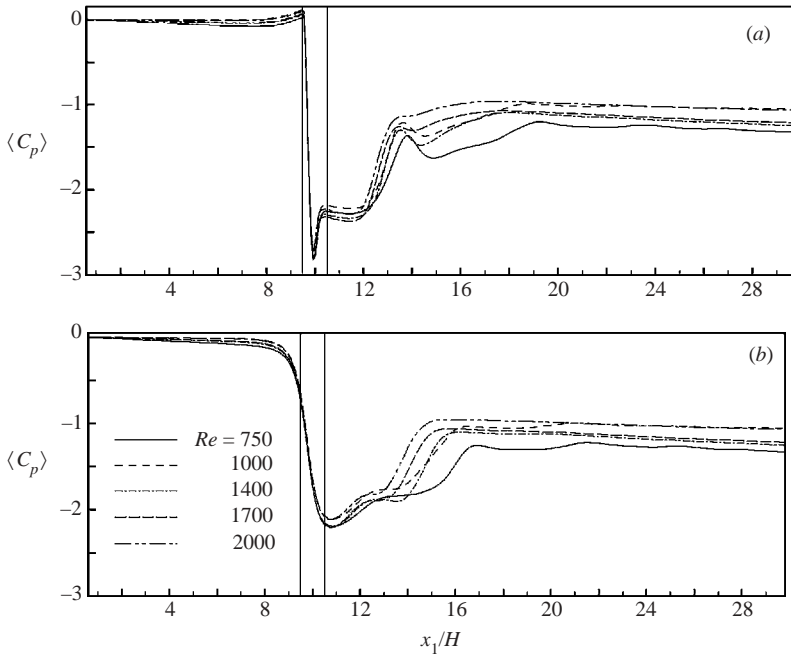


FIGURE 12. Mean pressure coefficient $\langle C_p \rangle$ on the channel walls. (a) Upper wall. (b) Lower wall. The two vertical lines in this and subsequent figures indicate the location and extent of the constriction.

Reynolds number and for $Re = 2000$, the extent of the recirculation region is about $2.8H$. As the Reynolds number increases, the boundary layer separating from the lip of the constriction rolls up closer to the constriction and this results in the decrease of the extent of the recirculation region. A smaller recirculation bubble is also observed to form on the lower wall and this is associated with the separation of the boundary layer from the bottom wall. This recirculation bubble also moves closer to the constriction with increasing Reynolds number and this is a direct result of the corresponding reduction in the size of the recirculation region on the upper wall.

Figure 12 shows the distribution of the mean pressure coefficient $\langle C_p \rangle$ on the upper and lower walls. This is defined as $\langle C_p \rangle = 2(p - p_{in})/\rho V_{max}^2$ where p and p_{in} are the pressure, and inlet static pressures, respectively. The variation of the upper-wall mean

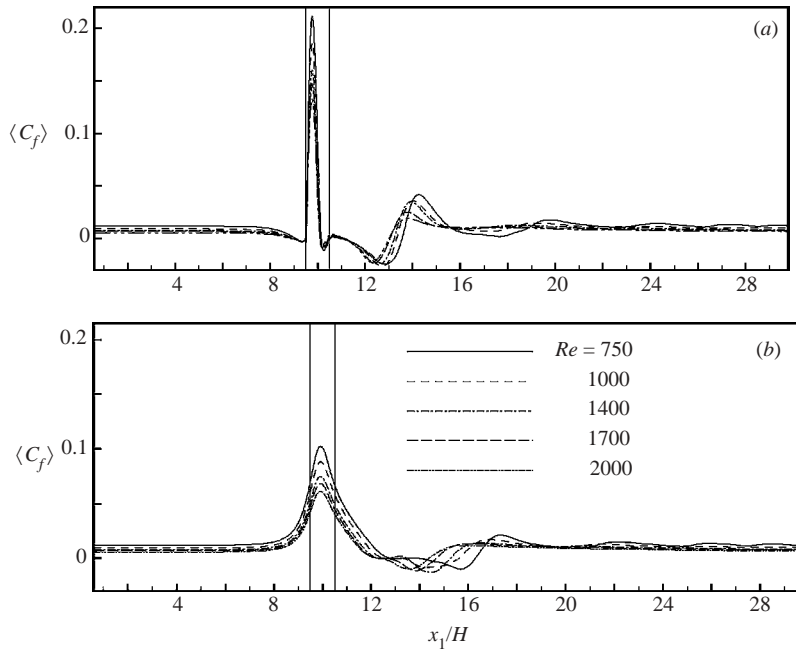


FIGURE 13. Mean skin friction coefficient $\langle C_f \rangle$ on the channel walls. (a) Upper wall. (b) Lower wall.

pressure coefficient can be interpreted directly in the context of the mean streamline pattern shown in figure 11. At $x_1/H = 9$, the flow first enters the constriction and the increase in velocity results in a steep drop in the pressure coefficient which reaches the minimum value at the lip of the stenosis at $x_1/H = 10$. Beyond this point, the flow enters the expansion and the pressure coefficient exhibits a steep increase. However, because of this strong adverse pressure gradient, the boundary layer on the upper wall separates at about $x_1/H = 10.5$. The flow expansion is effectively halted by the separation of the boundary layer and this produces a plateau in the pressure coefficient between $x_1/H = 10.5$ and 12.5 . As the separated shear layer attaches to the upper wall, the flow experiences expansion again which results in a sharp increase in pressure coefficient between $x_1/H = 12.5$ and 14 . This adverse pressure gradient results in the separation of the boundary layer on the lower wall and the small recirculation bubble located on the lower wall is associated with this separation process. The presence of this small recirculation bubble in the mean flow reduces the effective area of the channel and the resulting flow acceleration produces a drop in the static pressure which is most apparent for $Re = 750$ at around $x_1/H = 15$. The pressure coefficient on the lower wall shows similar behavior although the pressure gradients are not as high as for the upper wall.

As pointed out earlier, mean wall shear plays an important role in arterial disease and in figure 13 is shown the distribution of mean skin friction coefficients $\langle C_f \rangle$ on the upper and lower walls. This is defined as $\langle C_f \rangle = 2\langle \tau_w \rangle / \rho V_{max}^2$ where τ_w is the wall shear stress. On the upper wall, the largest magnitude of skin friction is found near the lip of the constriction which is consistent with the high mean velocity at this streamwise location. Downstream of the constriction, the shear stress becomes negative and this is associated with the presence of the large mean recirculation

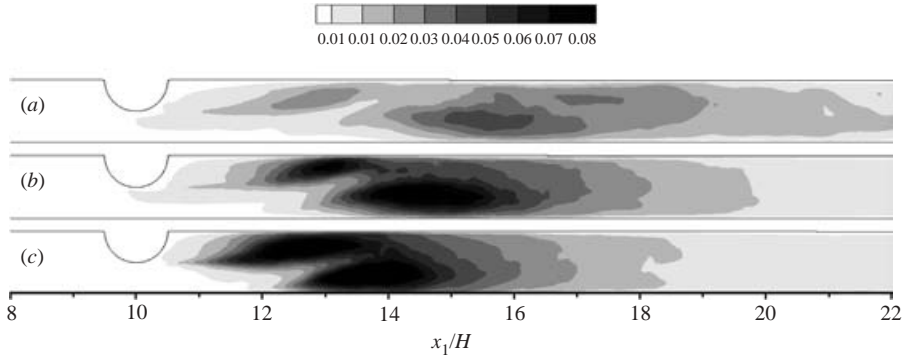


FIGURE 14. Contour plot of turbulent kinetic energy $\langle u_i''u_i'' \rangle/2$ for various cases. (a) $Re = 750$. (b) $Re = 1400$. (c) $Re = 2000$.

region on the upper wall. As the high-speed flow coming through the constriction attaches to the upper wall, it results in an increase in the skin friction and the local maxima in $\langle C_f \rangle$ at about $x_1/H = 14$ is due to this phenomenon. Downstream of this region, the flow begins to revert back to a nominal pulsatile flow in a channel and the skin friction values are fairly uniform and similar to those on the wall upstream of the constriction. The curve corresponding to $Re = 750$ clearly shows some undulations which are indications of the alternate separation/reattachment process that was described earlier in the paper. A similar behavior is also observed on the lower wall although, as for the wall pressure, streamwise gradients in the skin friction are also significantly lower than those observed on the upper wall.

4.3. Fluctuation characteristics

Figure 14 shows contour plots of the turbulent kinetic energy per unit mass which is defined as $\langle u_i''u_i'' \rangle/2$ non-dimensionalized by V_{max}^2 for the $Re = 750, 1400$ and 2000 cases. First, for all cases, it is observed that there are two distinct regions of increased turbulence activity and these are associated with the two shear layers that separate from the upper and lower walls. Secondly, as expected, the intensity of the turbulent fluctuations increases with Reynolds number. On the other hand, the streamwise extent of the region of intense turbulent fluctuations is found to reduce with increasing Reynolds number. This is because as the Reynolds number increases, both the separated shear layers become more unstable and roll up into vortices at an increasingly earlier stage. Since the turbulent fluctuations are associated with the breakup of these vortices, earlier vortex roll-up is accompanied with an upstream advancement of the regions of high turbulence activity. It is also worth pointing out that for $Re = 1700$ and 2000 , there is a close correlation between regions of high turbulent fluctuations and those of high SGS eddy viscosity (as shown in figure 6). This re-emphasizes the favourable quality of the dynamic SGS model of adding dissipation not in an *ad hoc* manner, but only in regions where there is significant activity in the small scales.

Figure 15 shows profiles of the turbulent kinetic energy at a number of streamwise locations for $Re = 750, 1400$ and 2000 . The key feature of this plot is that even though the turbulent kinetic energy is significantly lower for $Re = 750$ in the regions where the shear layer form, at $x_1/H = 19$ which is $9H$ downstream of the constriction, the magnitude and shape of the turbulent kinetic energy variation is similar for all

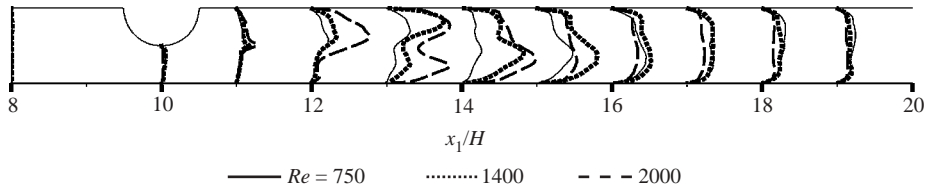


FIGURE 15. Profiles of the turbulent kinetic energy at various streamwise locations for $Re = 750, 1400$ and 2000 .

the cases. This implies that increased turbulence intensity is accompanied by an increase in dissipation at higher Reynolds number. This tends to diminish the intensity of the turbulent fluctuations so much that beyond about ten channel heights downstream of the constriction, flows at all Reynolds numbers exhibit similar turbulent fluctuation characteristics. This observation indicates that for a given stenotic severity, variability in the Reynolds number (which may for instance be due to a difference in the arterial diameter or blood pressure) produces a turbulent flow which is different only in the near vicinity of the stenosis. Further downstream, the turbulent flow develops a more universal character which is independent of the Reynolds number.

There is strong evidence to suggest that post-stenotic dilatation is due to arterial damage caused by pressure fluctuations associated with the complex unsteady flow created in this region (Lighthill 1975). Furthermore, wall pressure fluctuations are a key ingredient in acoustical techniques for detecting arterial stenosis such as phonoangiography (Ask *et al.* 1995). In this technique, sound caused by wall pressure fluctuations that are transmitted through the arterial wall and the surrounding tissue, is detected using an externally placed transducer. Subsequently, the intensity and frequency content of the sound is analysed in order to estimate the severity of the stenosis. Correlating the pressure fluctuation intensity with the vortex dynamics and understanding the effect of various flow parameters on the pressure fluctuations is therefore of relevance to this and other non-invasive acoustical detection techniques.

In figure 16 we have plotted the distribution of the coefficient corresponding to the root-mean-square pressure fluctuation, which is defined as $C_p'' = 2\langle p''^2 \rangle^{1/2} / \rho V_{max}^2$, on the upper and lower walls, respectively, for $Re = 750, 1400$ and 2000 . Note that p'' is the fluctuation away from the phase average and represents fluctuation with frequencies much higher than the pulsation frequency. Focusing first on the upper wall, we find that the dominant peak in wall pressure fluctuation occurs in the range $13 < x_1/H < 14$ for all the cases. A mechanism for the production of these large wall pressure fluctuations is evident from figures 7–9 which indicate that the region $13 < x_1/H < 14$ is precisely where the upper shear layer reattaches to the upper wall. Interaction with the wall combined with the inherent instability of the shear layer leads to the formation of smaller vortex structures which cause the wall pressure fluctuations. This observation is in line with the experiments of Tobin & Chang (1976) who also associated the peak in the intensity of wall pressure fluctuation with the reattachment of the shear layer. Apart from this similarity, the variation of the pressure fluctuation for $Re = 2000$ is quite different from the two lower-Reynolds-number cases. The peak pressure fluctuation for both $Re = 750$ and 1400 is sharp whereas that for $Re = 2000$ is more broad. This is consistent with the fact that at lower Reynolds numbers, the shear layer is expected to exhibit less cycle-to-cycle and spanwise variations in the location where it reattached to the wall. As the Reynolds number

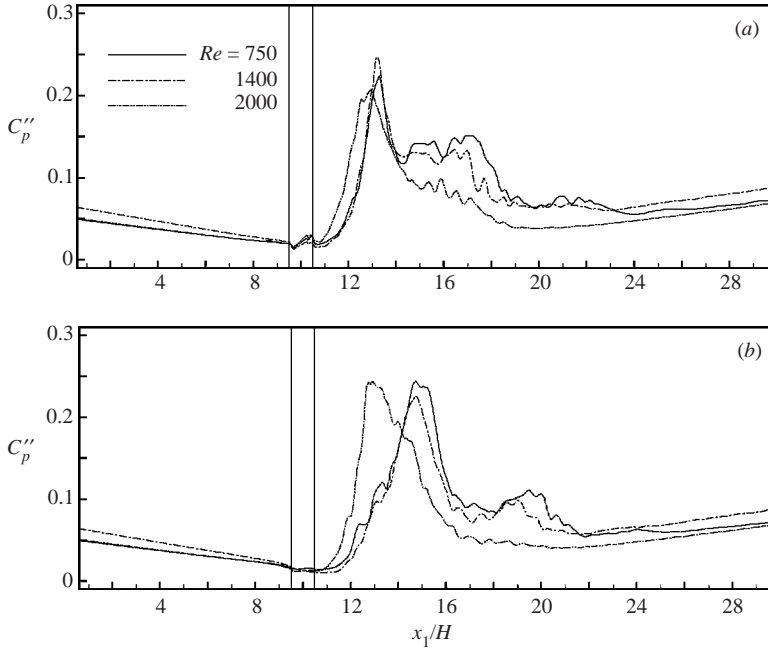


FIGURE 16. Root-mean-square pressure fluctuation $C_p'' = 2\langle p''^2 \rangle^{1/2} / \rho V_{max}^2$ on the channel walls. (a) Upper wall. (b) Lower wall.

increases to 2000, the shear layer becomes more chaotic and exhibits a larger cycle-to-cycle and spanwise variation in the reattachment location and this results in a broader peak in the wall pressure fluctuations. Another significant difference between $Re = 2000$ and the other two cases is that the wall pressure fluctuation shows only one clear maxima for $Re = 2000$ whereas for both the lower-Reynolds-number cases it shows another region of increased wall pressure fluctuations around $x_1/H = 17$. Again, from figures 7(c) and 8(c) we find that this is the region where the upper shear layer undergoes its second reattachment to the upper wall. For $Re = 2000$, owing to increased disorder in the flow, the alternate separation/reattachment scenario is not observed and the flow does not exhibit a clear secondary peak.

Figure 16(b) shows the wall pressure fluctuation on the lower wall and this shows a number of characteristics that are different from those observed at the upper wall. First, the peak fluctuation for $Re = 2000$ occurs at around $x_1/H = 13$ whereas for the two lower Reynolds numbers, the peak is located at around $x_1/H = 15$. Again, the increased wall pressure fluctuations can be correlated with the vortex dynamics. As is clear from figures 7(c) and 8(c), for $Re = 750$ and 1400, the lower shear layer rolls up into a large vortex at around $x_1/H = 15$. This vortex then disintegrates into smaller scale structures in the vicinity of the wall and velocity fluctuations associated with these vortex structures produce the wall pressure fluctuation in this region. For $Re = 2000$, the vortex dynamics is quite different. The lower shear layer rolls up into a small but intense vortex at around $x_1/H = 12.5$ (figure 9c) and immediately collapses into smaller scale structures. Consequently, the peak wall fluctuation for $Re = 2000$ occurs at around $x_1/H = 13$. Finally, as with the upper wall, the two lower-Reynolds-number cases show a secondary peak in the wall pressure fluctuation in the region $19 < x_1/H < 20$ whereas $Re = 2000$ shows no such peak. As before,

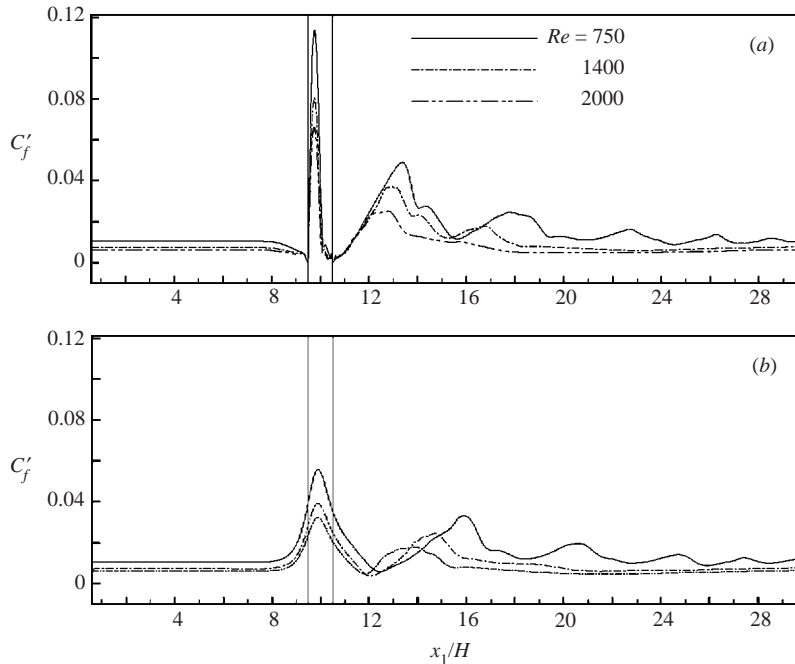


FIGURE 17. Root-mean-square skin friction coefficient $C'_f = 2\langle\tau_w'^2\rangle^{1/2}/\rho V_{max}^2$ on the channel walls. (a) Upper wall. (b) Lower wall.

as can be seen from figures 7 and 8, the lower shear layer undergoes its second separation–reattachment process in this region thereby causing an increase in the wall pressure fluctuation. Figure 9 for $Re = 2000$ does not indicate any such activity.

In addition to the wall pressure fluctuations, fluctuations in the wall shear stress may play an important role in the initiations and progression of arterial disease. Thus, accurate prediction of this quantity along with an understanding of the mechanisms/events that produce high levels of wall shear stress fluctuations is useful. Figure 17 shows the variation of coefficient of fluctuating wall stress defined as $C'_f = 2\langle\tau_w'^2\rangle^{1/2}/\rho V_{max}^2$ on the upper and lower walls, respectively, for $Re = 750$, 1400 and 2000. Note that τ_w' is the fluctuation away from the mean and includes the cycle-to-cycle fluctuations in this quantity. Thus, upstream of the stenosis where the fluctuation is primarily due to the cyclical oscillation in the inflow velocity, the variation of this quantity provides a direct, baseline measure of the wall shear stress fluctuation that would be present in an unconstricted channel. For all cases, a large peak in the fluctuating wall shear is found on the upper wall just upstream of the lip of the constriction which is primarily due to the cyclical variation in the flow velocity. Downstream of the constriction, the wall shear exhibits a more complex variation, but clear trends emerge with increasing Reynolds number. First, all cases show two or more peaks in the wall stress fluctuation downstream of the constriction. The first peak, which is also the dominant peak in the post-constriction region for all cases, occurs at about $x_1/H = 13.5$ for $Re = 750$ and shifts upstream monotonically with Reynolds number to about $x_1/H = 12.8$ for $Re = 2000$. This peak is clearly associated with the location where the upper shear layer attaches to the upper wall and the upstream shift of the peak with increasing Reynolds number is due to the shortening

of the shear layer and earlier roll-up. Also visible for $Re = 750$ are a series of smaller peaks further downstream at about $x_1/H = 18, 22.8, 26.2$ and 28.5 which are a clear signature of the alternate separation/reattachment process described earlier in the paper. Smaller peaks are also visible at higher Reynolds numbers; however, as Reynolds number increases, these peaks diminish in strength. In fact for $Re = 2000$, no clear peak downstream of the dominant peak at $x_1/H = 12.8$ is clearly visible. Instead, there is a region of slightly increased wall shear fluctuation up to about $x_1/H = 18$ beyond which the fluctuation level returns to a level comparable to that of the flow upstream of the constriction.

Figure 17(b) shows the corresponding shear stress fluctuation level on the lower wall. In general, the peak shear stress fluctuation level on the lower wall which occurs at about $x_1/H = 10$ is half the value at the upper wall. As with the upper wall, a second peak in shear stress fluctuation is present downstream of the constriction for all cases. The peak is located at about $x_1/H = 16$ for $Re = 750$ and shifts steadily upstream with increasing Reynolds number such that at $Re = 2000$, it is located at about $x_1/H = 14$. This peak is also associated with the location where the shear layer that separates from the lower wall, rolls up into a vortex. As the Reynolds number is increased, the vortex roll-up occurs further upstream and, consequently, this peak also shifts upstream. Furthermore, as with the upper wall, additional smaller peaks are present further downstream at the lower Reynolds numbers and these are also a consequence of the alternate separation/reattachment of the lower shear layer.

From a pathological view point, the variation in the shear stress fluctuation level observed here may have several important implications. First, the higher shear stress fluctuation level on the upper wall might indicate that for a non-symmetric stenosis, greater instance of pathological behaviour in the endothelial cells may occur on the side of the wall on which the stenosis is the thickest. Furthermore, at lower Reynolds numbers, this behaviour may occur at a number of localized regions downstream of the stenosis whereas at higher Reynolds numbers, the damage will occur primarily in one localized region.

4.4. Spectral analysis

In this section, we focus on analysing the temporal variations and frequency spectra of the velocity and pressure in the region downstream of the constriction. As in many previous investigations, this analysis is primarily aimed at addressing two issues, the first being the spectral dynamics in pulsatile post-stenotic flows and the second, the origin and interpretation of sounds associated with the unsteady post-stenotic blood flow. The spectral dynamics of the $Re = 2000$ case is described in detail and this is then used as a baseline to compare the changes in the observed spectral signature of the flow as the Reynolds number is reduced to 750. At any given (x_1, x_2) location, the frequency spectrum is computed at all the grid points along the homogeneous spanwise direction and then averaged over the span.

Figure 18 shows the temporal variations of the streamwise velocity (u_1) at the channel centreline at seven different streamwise locations downstream of the constriction and figure 19 shows the corresponding velocity fluctuation u_1'' at these locations. In these two plots, ϕ denotes the phase in the pulsation and this has been arbitrarily set to zero at the beginning of one cycle where $Q(t) = 0$. Furthermore, figure 20 shows the frequency spectrum corresponding to the variation of u_1'' . It should be noted that the temporal variations shown in figures 18 and 19 are at a fixed spanwise station whereas the frequency spectra is obtained by averaging the individual spectra at a particular (x_1, x_2) location across the span. The frequency

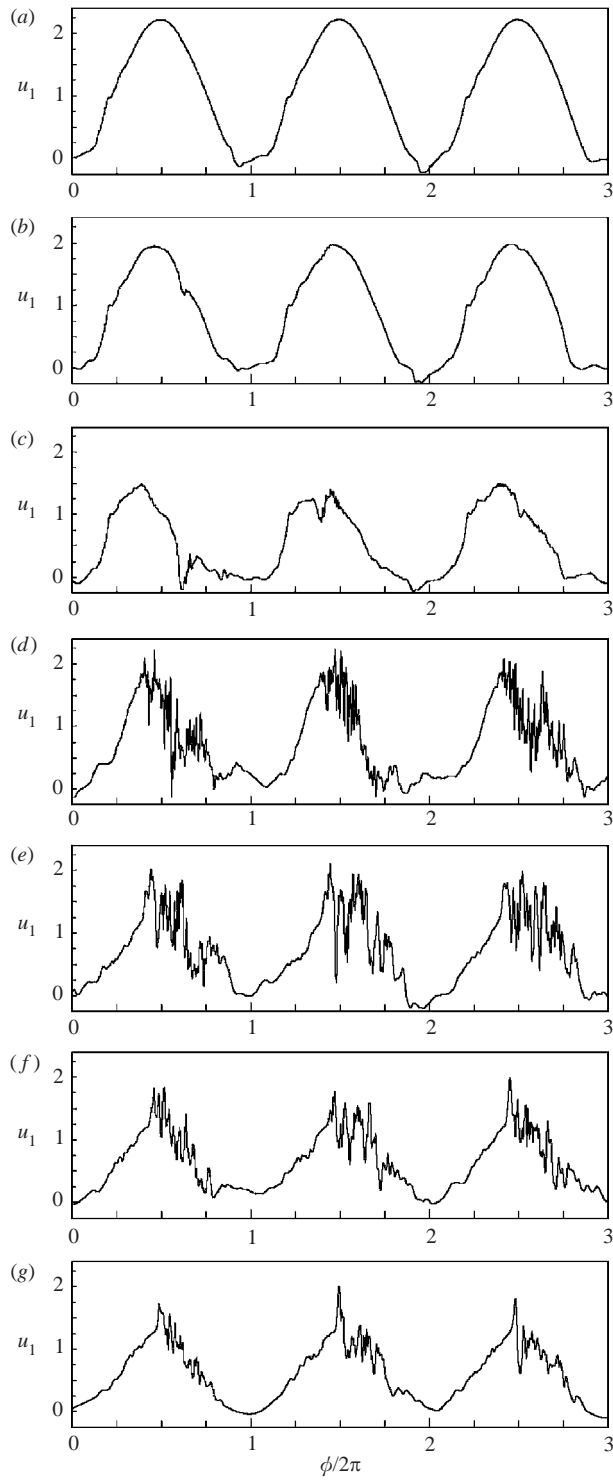


FIGURE 18. Temporal variation of u_1 at various location downstream of the constriction along $x_2/H = 0.5$ and $x_3/H = 0$ for $Re = 2000$. (a) $x_1/H = 10.46$, (b) 10.63, (c) 10.85, (d) 12.05, (e) 14.53, (f) 15.73, (g) 17.43.

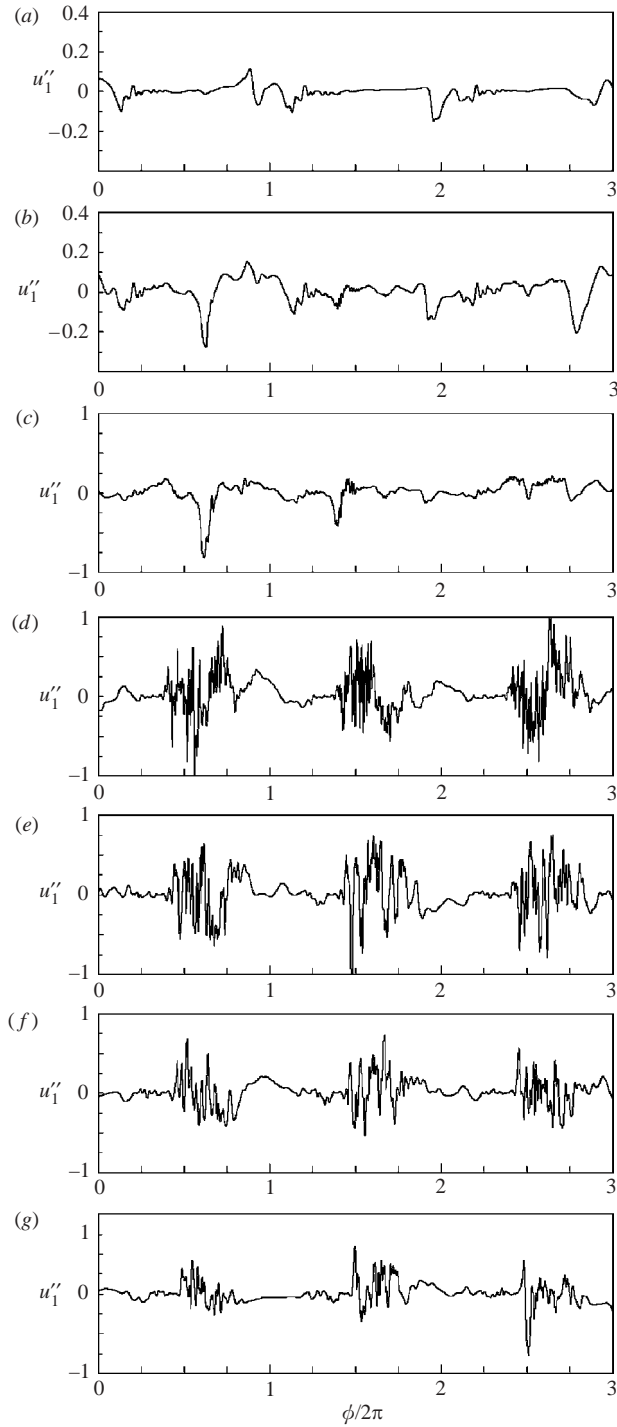


FIGURE 19. Temporal variation of u''_1 at various location downstream of the constriction along $x_2/H = 0.5$ and $x_3/H = 0$ corresponding to previous figure. (a) $x_1/H = 10.46$, (b) 10.63, (c) 10.85, (d) 12.05, (e) 14.53, (f) 15.73, (g) 17.43. Note the different scale for the y-axis on (a) and (b).

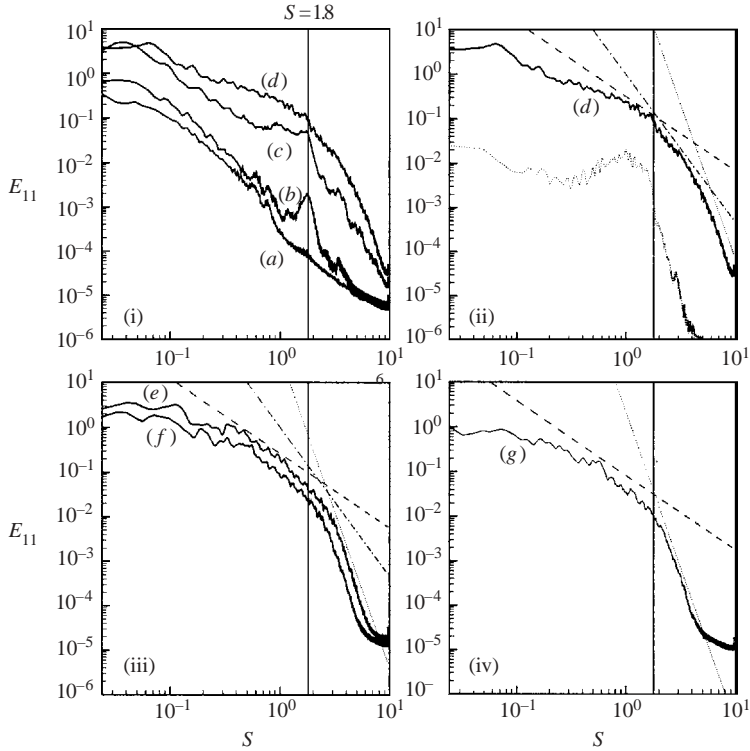


FIGURE 20. Frequency spectra corresponding to the temporal variation of u_1'' shown in figure 19. Each curve is marked with a letter which denotes the location of the point *vis-à-vis* figure 19. Note that dotted, dashed and dash-dot straight lines correspond to S^{-7} , $S^{-5/3}$ and $S^{-10/3}$ variations, respectively. (i) Spectra at locations corresponding to (a), (b), (c) and (d). (ii) Spectra at location (d) replotted to facilitate detailed comparison with empirical scalings. Dotted line in this plot corresponds to the location near the bottom wall at $x_1/H = 12.05$. (iii) Spectra at location (e) and (f). (iv) Spectra at location (g).

in these plots has also been non-dimensionalized by V_{max}/H and denoted by the symbol S .

Figures 18(a), 19(a) and 20(a) correspond to location $x_1/H = 10.46$ which lies upstream of the region where the vortex roll-up occurs (see figure 9). At this location, the velocity variation is mostly sinusoidal. The u_1'' plot at this location indicates that the variation is highly repeatable from cycle to cycle except for a relatively small fluctuation at the beginning of the pulsation. The corresponding frequency spectra in figure 20 show no distinct peaks, indicating that the flow at this location is laminar and almost strictly cyclical.

Figures 18(b) and 19(b) show the temporal variation of u_1 and u_1'' , respectively, at $x_1/H = 10.63$. The variation of u_1 looks similar to that at the previous location, however, the plot of u_1'' reveals some key differences. Figure 19(b) shows that there are significant cycle-to-cycle variations in the velocity at this location and these fluctuations are almost uniformly spread over the entire cycle. Although visual inspection of the velocity variation does not indicate any periodicity in the velocity fluctuation (at least at this one particular spanwise station) the frequency spectrum shows the presence of a distinct peak with a frequency corresponding to $S = 1.8$. Careful examination of the vorticity field (shown in figure 9) indicates that the

observed high frequency is associated with the formation of Kelvin–Helmholtz type rollers in the shear layer that separates from the lip of the constriction.

As pointed out before, a number of previous experimental studies have observed and characterized the periodic formation of vortex structures in such flows. In particular, Cassanova & Giddens (1978) investigated the vortex-shedding phenomena downstream of an axisymmetric constriction in a circular pipe with sinusoidally varying pulsatile inflow. In their study, the area constriction ratio d^2/D^2 (where D is the unoccluded pipe diameter and d is the diameter of the occluded section) was equal to 0.5 and 0.25, the Reynolds number (based on D and maximum inlet velocity) was 2540 and the Womersley frequency parameter ($D\sqrt{2\pi/T}\nu/2$ where T was the time-period of the pulse) was equal to 15. Thus, the Reynolds numbers, constriction ratio and pulsatile waveform are comparable to this particular simulation and therefore, despite the other differences, it is worthwhile making a comparison between the two.

Based on the discussion in the paper of Cassanova & Giddens (1978), the shedding frequency (f) non-dimensionalized by u_j/d , where u_j is the peak section-averaged flow velocity through the constriction, is in the range of 0.5–1 for the $d^2/D^2 = 0.5$ stenosis. Lu *et al.* (1983) who investigated the flow downstream of an axisymmetric constriction in a pipe with steady inflow at a Reynolds number (based on pipe diameter and maximum inlet velocity) of about 17 000 also found a non-dimensional vortex-shedding frequency (fu_j/d) ranging from about 0.5 in the near vicinity of the constriction to about 0.1 further downstream. A similar non-dimensionalization (i.e. with h and peak section-averaged velocity through the constriction which is equal to (HV_{max}/h)) of the vortex-shedding frequency yields a value of 0.45 for the current simulation which is in reasonable agreement with the experimental results of both these studies. This indicates that the vortex shedding observed in the current simulation is a robust phenomena that is characteristic of these flows notwithstanding the differences in the geometry and other features of the flow configuration.

Figures 18(c) and 19(c) show the temporal variation further downstream of the constriction at $x_1/H = 10.85$. This location is downstream of the position of initial roll-up of vortices and lies in the region where the vortices grow in size and start interacting with the vortex structures in the recirculation region. The variation of u_1'' is similar to that observed at the previous location although the magnitude is considerably larger. This is a clear indication of the rapid growth of the vortex structures as they convect downstream in this region. The corresponding frequency spectra in figure 20(c) does not indicate a distinct peak at the vortex-shedding frequency of $S = 1.8$, but does show a rapid roll-off in the energy beyond this frequency. The absence of a distinct peak in the frequency spectrum is an indication of the growing complexity of the vortex structures as they convect downstream in this region.

Figures 18(d) and 19(d) show the temporal variation at $x_1/H = 12.05$. In the context of the vorticity plot shown in figure 9(c), this location can be identified with the downstream end of the shear layer that separates from the lip of the stenosis. In this region, the vortex structures have grown to a size that is comparable to that of the constriction and begin interacting with the upper channel wall. The temporal variation shows a marked change from the previous locations. In particular, each cycle exhibits a duration of high-intensity complex fluctuation followed by a period of low-level activity. The period of intense fluctuations begins at about $\phi/2\pi = 0.35$ and ends at about $\phi/2\pi = 0.8$. The rest of the cycle is a period of relatively reduced fluctuation intensity. Thus, a significant portion of the high-intensity fluctuations occurs during the deceleration phase of the cycle and this is consistent with the

previous experimental observations (Khalifa & Giddens 1981; Lieber & Giddens 1990; Cassanova & Giddens 1978). The corresponding frequency spectra plotted in figure 20(i) when compared with the spectra at the previous locations indicates a fuller spectrum characteristic of a transitional flow.

In order to facilitate further analysis, the spectrum at this location has been plotted in figure 20(ii). In these and subsequent plots, we have also included lines corresponding to $S^{-5/3}$, $S^{-10/3}$ and S^{-7} . The $S^{-5/3}$ variation is associated with the well-known inertial subrange (Tennekes & Lumley 1972). A noticeable inertial subrange in the spectra indicates a well-developed turbulent flow. The S^{-7} variation on the other hand characterizes the dissipation range (Hinze 1975) where energy decay is dominated by viscous forces. The inclusion of the $S^{-10/3}$ line is motivated by previous investigations of post-stenotic flow by Kim & Corcoran (1974) and Lu *et al.* (1980) who found evidence of such a range in the velocity spectra of post-stenotic flows. In particular, Lu *et al.* (1980) who obtained *in vivo* measurements of post-stenotic flows found that the velocity spectra rolled off from a $-5/3$ to a $-10/3$ slope at a distinct frequency which was associated with the arterial murmur. In the current study also, we investigate the presence of these spectral ranges in order to compare the current results with these previous studies. Careful examination reveals that the spectra at $x_1/H = 12.05$ do show a change in slope at about $S = 1.8$. Comparison with the various frequency scalings indicates that between $S = 1.8$ and 3.0 , the spectrum follows a $-10/3$ variation and then gradually rolls off to a -7 slope at higher frequencies. Below $S = 1.8$, the slope of the spectrum is clearly less than $-10/3$. Between $S = 0.7$ and 1.8 , the slope of the spectrum matches favourably with the $-5/3$ line although this match is tenuous at best.

Figures 18(e, f) and 19(e, f) correspond to locations $x_1/H = 14.53$ and 15.73 , respectively, and both these locations exhibit similar behaviour. The period of high-intensity fluctuation still occurs roughly between $\phi/2\pi = 0.35$ and 0.8 at these two locations, but the reduction in the intensity of fluctuation with downstream distance is apparent, especially at $x_1/H = 15.73$. The frequency spectra for these two locations are shown in figure 20(iii). The key difference between these and the spectra at the previous location is the absence of the $-10/3$ range. At these two locations, the spectra shows a $-5/3$ range that extends from about $S = 0.4$ to 1.0 . Beyond this frequency, the spectra rolls off gradually and attains a slope of -7 at around $S = 3.0$.

Finally in figures 18(g) and 19(g) show the temporal variations of the velocity at $x_1/H = 17.43$. As can be seen from figure 9, this location is far downstream of the region which is dominated by the shear layers from the upper and lower walls. At this downstream location, the velocity fluctuations are of a much lower magnitude and furthermore, the intense activity occurs in a shorter duration ranging from $\phi/2\pi = 0.5$ to 0.8 . The frequency spectra corresponding to this location has been plotted separately in figure 20(iv). Examination of this spectrum reveals that it closely follows a $-5/3$ slope from $S = 0.2$ to 1.8 and rolls off rapidly to a -7 slope beyond that. The relatively large inertial subrange is indicative of a well-developed turbulent flow in this region. Furthermore, even though this location is far enough downstream that it is not under the direct influence of the shear-layer vortices, the roll-off in the spectrum from a $-5/3$ to -7 slope at roughly $S = 1.8$ indicates that the spectral dynamics is still governed by the fluctuations associated with the shear-layer vortices.

In general, the current data support previous experiments of post-stenotic flows that have found these various regimes in the frequency spectra of post-stenotic flows. The fact that the current planar stenosis model produces results that are in line with

experiments carried out *in vitro* in axisymmetric configurations as well as *in vivo* studies again supports the assertion that the general flow features of post-stenotic flows are relatively insensitive to the details of the geometric configuration.

Analysis of the velocity fluctuation and spectra allows us to connect the spectral dynamics with the dynamics of the vortex structures. Furthermore, the presence and extent of the inertial subrange in the velocity spectra provides a straightforward indication of how well established the turbulence is in the flow downstream of the constriction. However, the characteristics of the sound produced by post-stenotic flows (arterial murmurs) are governed not by the velocity fluctuation but by the pressure fluctuations. In particular, it is the wall pressure fluctuations that are transmitted through the arterial walls and surrounding tissue and detected externally as an audible acoustic signal. Thus, analysis of the pressure fluctuations and corresponding spectra should provide some insight into the characteristics of sounds produced by post-stenotic flows. With this as motivation, we examine the pressure fluctuation and corresponding frequency spectra both in the midstream and upper and lower walls.

Figure 21 shows the pressure fluctuation (p'') non-dimensionalized by $\rho V_{max}^2/2$ at the same seven midstream locations for which the velocity fluctuation is shown in figure 19. The corresponding frequency spectra are shown in figure 22. The first location at $x_1/H = 10.46$ is upstream of where the shear-layer vortices are formed and at this location, the pressure fluctuations shown in figure 21(a) are relatively small and distributed evenly throughout the flow cycle. The frequency spectra at this location show a small but distinct peak at $S = 1.8$ which has been established as the vortex-shedding frequency for this particular flow. This is indicative of the elliptic nature of the pressure field which senses vortex structures that form periodically further downstream.

Figure 21(b) shows the pressure fluctuation at $x_1/H = 10.63$. Although no pattern of periodicity can be discerned in these fluctuations, it is noted that the fluctuation level is somewhat higher around midcycle, i.e. around $\phi/2\pi = 0.5$. The corresponding frequency spectrum shows a large and distinct peak at the vortex-shedding frequency of $S = 1.8$ and this is commensurate with the peak observed in the velocity spectrum at this location.

Figure 21(c) shows the pressure fluctuation at $x_1/H = 10.85$, and at this location there is a significant increase in the fluctuation level. The period of increased activity is centred around the midcycle with large cycle-to-cycle variation in the pattern of fluctuations. The corresponding frequency spectrum shows two distinct peaks, one at $S = 1.8$ and the other at about $S = 1.1$. We believe that this somewhat lower frequency is associated with the periodic formation of vortices in the shear layer that separated from the lower wall. The velocity spectra near the lower wall at $x_1/H = 12.05$ which is shown in figure 20(ii) also exhibits a peak at around $S = 1.0$ and this supports our hypothesis. Thus, the dynamics of the flow downstream of this asymmetric constriction is governed by two incommensurate frequencies and this is expected to produce complex dynamical behaviour in the flow downstream of this region.

Figure 21(d) shows the pressure fluctuation at $x_1/H = 12.05$ and, at this location, there is a significant increase in the fluctuation intensity and duration. There is a clear separation between periods of high and very low fluctuation activity with the former occurring almost exclusively between $\phi = 0.35$ and 0.85 in every cycle. The frequency spectrum at this location, which is shown in figure 22(i), does not exhibit any distinct peaks. However, it does exhibit a sharp roll-off beyond about $S = 1.2$ which is in line with the frequency of the lower shear layer.

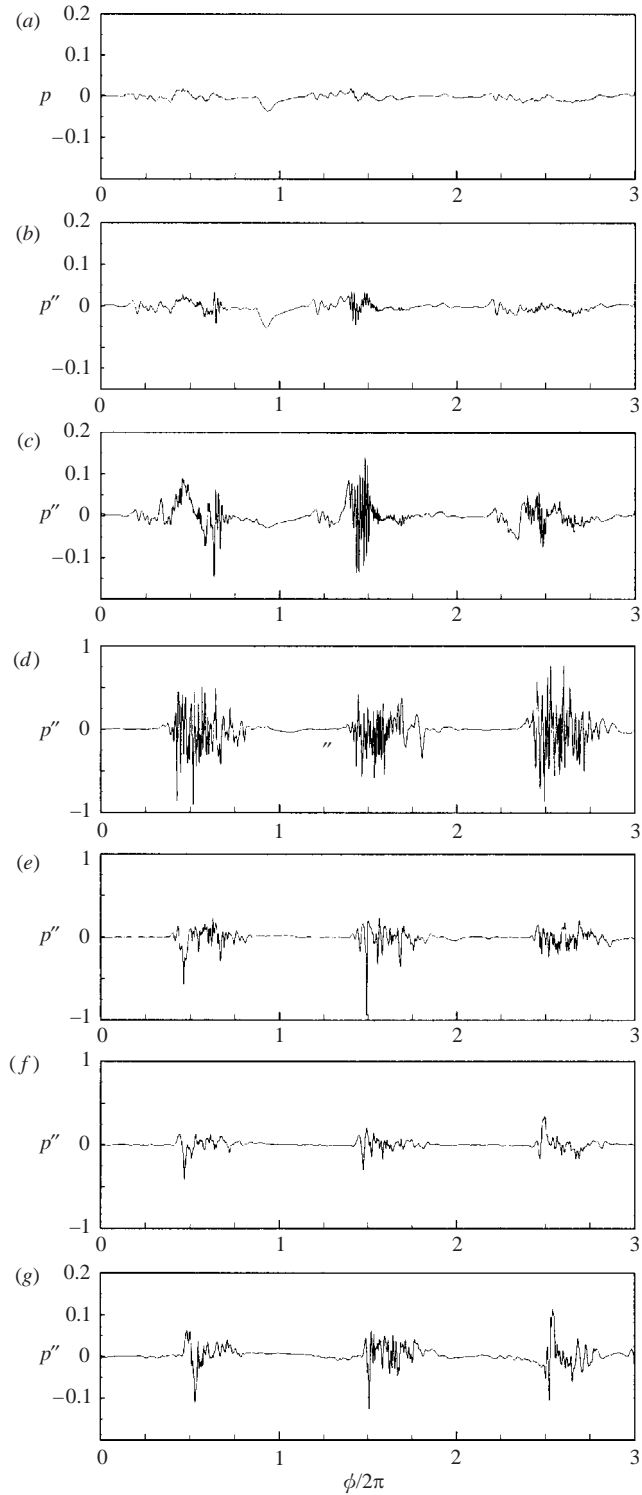


FIGURE 21. Temporal variation of p'' at various locations downstream of the constriction along $x_2/H = 0.5$ and $x_3/H = 0$ for $Re = 2000$. (a) $x_1/H = 10.46$, (b) 10.63, (c) 10.85, (d) 12.05, (e) 14.53, (f) 15.73, (g) 17.43. Note the different scale for the y-axis on (d), (e) and (f).

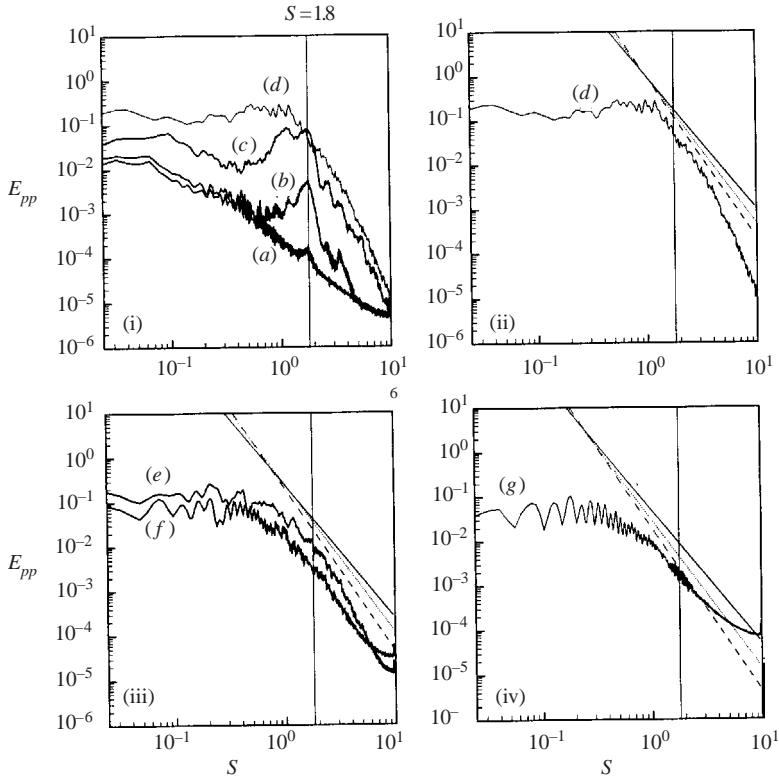


FIGURE 22. Frequency spectra corresponding to the temporal variations of p'' shown in figure 21. Each curve is marked with a letter which denotes the location of the point *vis-à-vis* the previous figure. Note that solid, dotted and dashed straight lines correspond to $S^{-7/3}$, $S^{-10/3}$ and $S^{-11/3}$, respectively. (i) Spectra at locations corresponding to (a), (b), (c) and (d). (ii) Spectra at location (d). (iii) Spectra at location (e) and (f). (iv) Spectra at location (g).

In the past, the scaling of the pressure spectra in post-stenotic flows has been investigated by a number of workers. In particular, previous investigations of Clark (1977) and Fredberg (1977) found that wall pressure spectra gradually approached a slope of $-10/3$ at higher frequencies. No physical justification for this scaling was provided, although it is likely that the basis for this lies in the $-5/3$ inertial range velocity spectrum and the quadratic dependence of pressure on velocity in inviscid flows. In an unrelated but relevant study, George *et al.* (1984) analysed the pressure spectra in homogeneous, turbulent free shear flow. The approach employed by them was to directly Fourier transform the integral solution to the Poisson equation for a homogeneous constant-mean-shear flow. The contribution to the pressure fluctuation spectrum was decomposed into turbulence–mean-shear interaction terms and a turbulence–turbulence interaction terms. Furthermore, assuming a $k^{-5/3}$ scaling in the velocity spectrum (where k is the wavenumber), it was shown that the turbulence–mean-shear interaction component of the pressure fluctuation, which would be dominant in the energy containing range, would scale as $k^{-11/3}$. On the other hand, the turbulence–turbulence interaction term, which would dominate the high-wavenumber portion of the spectra would scale as $k^{-7/3}$, a result they note has previously been obtained by Inoue (1954) and Batchelor (1953). In the case of an

anisotropic flow, they note that turbulence–mean-shear interaction will also produce a $k^{-9/3}$ type of scaling.

In comparing the scaling of the pressure fluctuations for the current flow with the analysis of George *et al.* (1984), a number of points must be noted. First, even though initial development of the shear layer that separates from the lip of the constriction occurs away from the channel walls, the flow downstream of the constriction cannot be classified as a free shear flow. In fact, this flow can be viewed as a pulsatile wall-bounded jet. Furthermore, the current flow is highly non-homogeneous in the region of interest. Thus, it is not clear how the presence of the wall and flow inhomogeneity will affect the scaling of the pressure spectra. However, despite these differences, the analysis of George *et al.* (1984) provides some analytical and physical background for the analysis of the pressure spectra. It is expected that comparison itself, whether favourable or not, will yield valuable insight into the dynamics of this flow.

In figure 22(ii), the pressure spectrum at $x_1/H = 12.05$ is plotted separately along with lines corresponding to $S^{-9/3}$, $S^{-10/3}$ and $S^{-11/3}$ scalings. None of the plots in this series showed any match with the $S^{-7/3}$ scaling, and therefore this scaling is not shown on these plots. Examination of the spectra reveals that within a frequency range from about $S = 1.2$ to about 3, the slopes of the spectra match best with the $S^{-11/3}$ line. The spectra at two downstream locations, $x_1/H = 14.53$ and 15.73, are plotted in figure 22(iii) along with lines representing the three different scalings. Again, careful examination reveals that between roughly $S = 1.8$ and 3.2 both spectrum are in best agreement with the $S^{-11/3}$ scaling. Finally, the spectrum at location $x_1/H = 17.46$ does not show any observable match with any of these three scalings. Thus, it may be concluded from these plots that there is fair evidence that the pressure spectrum in the mid-channel region shows some similarity to a free-shear flow. In particular, the inertial subrange matches best with the $S^{-11/3}$ scaling.

Since arterial murmurs are created by wall pressure fluctuations, it is also useful to analyse the spectrum of the pressure fluctuations on the upper and lower walls. However, at the walls, the comparison with the analysis of George *et al.* (1984) is not expected to be valid since the velocity and pressure fluctuations are most probably affected by the presence of the wall and show little resemblance to a free-shear flow. Since the region of highest pressure fluctuation intensity is expected to dominate the sound produced by the flow, here we focus only on this region of the wall. Figures 23(a) and 23(b) show the wall pressure fluctuations on the upper and lower walls, respectively, at $x_1/H = 13.06$ which is in the near vicinity of the peak in wall pressure fluctuation intensity as indicated by figure 16. Note that just as in the midstream locations, the pressure fluctuations at the wall also occur roughly between $\phi = 0.35$ and 0.85. During the rest of the cycle, the pressure fluctuation level is very much lower. However, the amplitude of the wall pressure fluctuations in these region is significantly higher than all the midstream locations examined earlier in this section.

Figure 24 shows the corresponding frequency spectra at these locations and a number of observations can be made regarding this plot. First, no distinct peak corresponding to the shedding frequency of either shear layers is observed in the wall spectra. The wall pressure spectrum on the lower wall shows a broad peak at around $S = 0.5$, whereas the corresponding spectrum for the upper wall exhibits no peak at all. However, both spectra exhibit a distinct roll-off at around $S = 1.0$ which is commensurate with the observed shedding frequency of the lower shear layer. For the lower wall, the spectrum beyond $S \approx 1$ rolls off with a well-defined slope of $-17/3$. In contrast, for the upper wall, the roll-off beyond $S \approx 1$ is gradual up to about $S = 3$

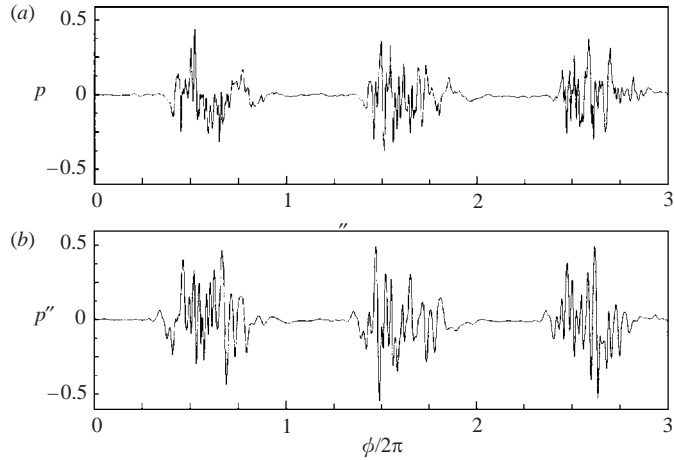


FIGURE 23. Temporal variation of p'' on the channels walls at $x_1/H = 13.06$ for $Re = 2000$ which corresponds to the region where the wall pressure fluctuation intensity is highest. (a) Upper wall. (b) Lower wall.

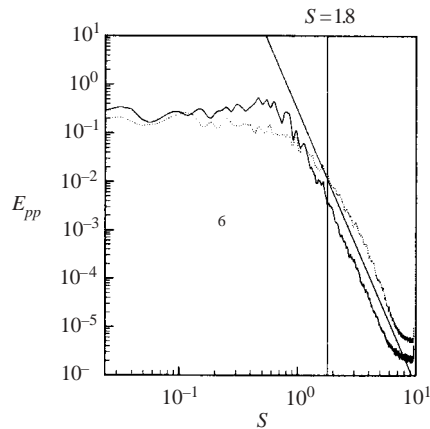


FIGURE 24. Frequency spectra corresponding to the temporal variations of p'' on the wall at $x_1/H = 13.06$ shown in figure 23. Dotted, upper wall; solid, lower wall. The solid straight line in the plot corresponds to $S^{-17/3}$.

and exhibits a sharper than $-17/3$ roll-off beyond this frequency. This more complex behaviour can be explained by noting that because of the upward deflection of the jet after the constriction, the upper wall is affected by the dynamics of both shear layers, whereas the lower wall is affected for the most part by only the lower shear layer. Thus, the upper wall pressure spectrum shows the effect of two energetic frequencies, whereas the lower wall pressure fluctuation corresponds only to the lower shear-layer dynamics. The physical and theoretical justifications for the observed $S^{-17/3}$ are not apparent at this time.

A limited set of results for the $Re = 1000$ case are presented in order to demonstrate the general similarity in the spectral behaviour between this and the $Re = 2000$ case. Figure 25 shows the frequency spectra of the streamwise velocity fluctuation (u''_1)

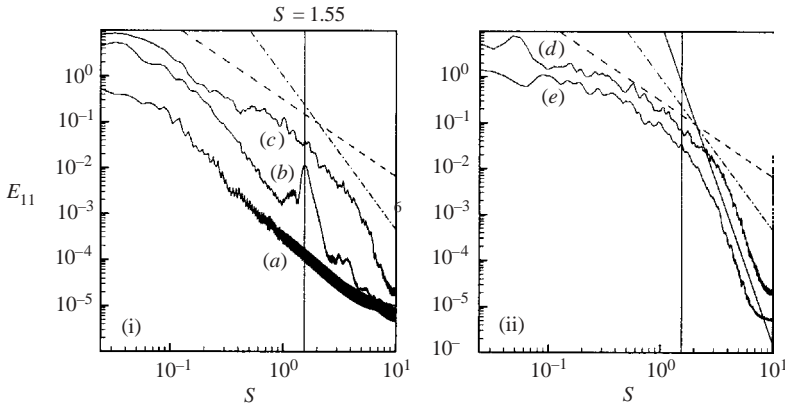


FIGURE 25. Frequency spectra corresponding to the temporal variation of u''_1 along the channel centreline for the $Re = 1000$ case. (i) Spectra at locations (a) $x_1/H = 10.41$, (b) 10.75 and (c) 12.05. (ii) Spectra at locations (d) $x_1/H = 14.00$ and (e) 17.55. The solid, dashed and dash-dot straight lines correspond to S^{-7} , $S^{-5/3}$ and $S^{-10/3}$, respectively.

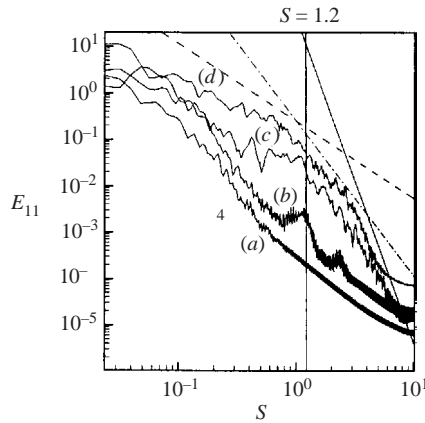


FIGURE 26. Frequency spectra corresponding to the temporal variation of u''_1 along the channel centreline for the $Re = 750$ case. Spectra at locations (a) $x_1/H = 10.65$, (b) 11.33, (c) 12.98 and (d) 17.16. The solid, dashed and dash-dot straight lines correspond to S^{-7} , $S^{-5/3}$ and $S^{-10/3}$, respectively.

along the channel centreline in the region downstream of the constriction. As in the $Re = 2000$ case, a distinct peak corresponding to the shear-layer vortex formation is observed at $x_1/H = 10.75$. The value of the peak frequency is, however, about $S = 1.55$ which is lower than the frequency observed for the $Re = 2000$ case. Further downstream, the peak disappears and the spectra broadens out. Examination of spectra at $x_1/H = 17.55$ indicates the presence of a relatively short $-5/3$ range from about $S = 0.5$ to 1.5. Beyond this range, the spectra rolls off and attains a -7 slope at higher frequencies.

Next, we present frequency spectra for the $Re = 750$ case which is the lowest-Reynolds-number case simulated here. Figure 26 shows the frequency spectra of the streamwise velocity fluctuation (u''_1) at four locations along the channel centreline

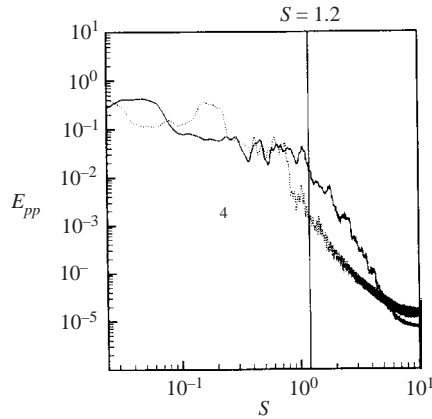


FIGURE 27. Wall pressure frequency spectra corresponding to $Re = 750$ case at locations where highest intensity of wall pressure fluctuations is found. Solid line, upper wall at $x_1/H = 13.48$; dotted line, lower wall at $x_1/H = 14.61$.

ranging from $x_1/H = 10.65$ to 17.16 . At $x_1/H = 11.33$, the spectrum indicates a peak at about $S = 1$. However, unlike the higher-Reynolds-number cases, the peak is quite broad and extends from about $S = 0.9$ to 1.2 . It should be pointed out that visualization of the vortex dynamics does not indicate clear vortex shedding at this Reynolds number, and it would seem that the peak in the spectra is caused by small-scale oscillations of the shear layer. Thus, the shear layer behaviour at this Reynolds number is somewhat different from that observed at the higher Reynolds number. Furthermore, the spectra further downstream does not show any match with a $-5/3$ slope, indicating that for the flow at this low Reynolds number there is no transition to turbulence.

Finally, figure 27 shows the wall pressure spectra at locations on the upper and lower walls where the intensity of pressure fluctuations is the highest. Also plotted is a vertical line corresponding to $S = 1.2$, which is the upper extent of the broad peak observed in the centreline velocity spectrum. On the upper wall, the pressure spectra clearly shows a sharp break in the vicinity of $S = 1.2$ which is in line with our observations of the $Re = 2000$ case. On the lower wall, the break in the spectrum occurs at about $S = 0.8$. It should be reiterated that for the $Re = 2000$ case, it was found that the characteristic frequency of the shear layer on the lower wall was lower than that of the upper wall and that the break in the wall pressure spectrum was associated with these characteristic frequencies. The wall pressure spectra for the $Re = 750$ case also shows a similar behavior.

In addition to the three cases for which data are presented in this section, the frequency spectra corresponding to the velocity and pressure fluctuations have also been analysed in detail for the $Re = 1400$ and 1700 cases. The analysis indicates that the shear-layer vortex-shedding frequencies for these two cases are about 1.63 and 1.72 , respectively. Thus, the shedding frequency is found to increase monotonically with Reynolds number and this is commensurate with the experimental study of Jones & Fronek (1987). Observed values of this non-dimensional frequency for all the cases are given in table 1. Based on the limited number of cases simulated here, an attempt has been made to extract an empirical correlation for the observed shear-layer vortex-formation frequency. Figure 28 shows a plot of $\log(S)$ versus $\log(Re)$ for the

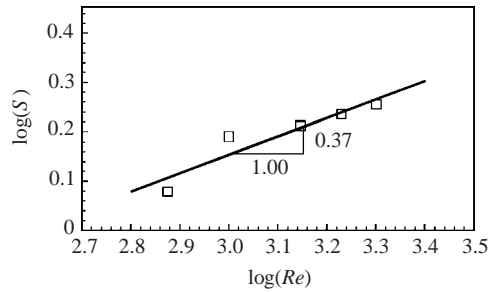


FIGURE 28. Plot of $\log(S)$ versus $\log(Re)$ for all cases presented here. Best fit (solid) line indicates that $S \propto Re^{0.37}$ for the range of parameters studied here.

various cases simulated here and a best-fit line through these points indicates that

$$S \propto Re^{0.37}$$

for this flow. The exponent in this correlation is found to be much lower than that put forward by Jones & Fronek (1987). However, this is not entirely unexpected owing to the difference between the two configurations (asymmetric planar in the current case versus axisymmetric for Jones & Fronek). In fact, if we compare shear-layer vortex-shedding frequency for cylindrical and axisymmetric bluff bodies, we find that frequency increase with Reynolds number is more rapid for the latter. In particular, for circular cylinders $S \propto Re^{0.67}$ (Prasad & Williamson 1996), whereas for spheres, a fit through well-established experimental data (Sakamoto & Haniu 1990) in the range $800 < Re < 2000$ indicates that the Strouhal number of shear-layer vortex shedding is proportional to $Re^{1.0}$.

5. Conclusions

Direct numerical simulation and large-eddy simulation have been used to study pulsatile flow in a channel with a one-sided semicircular constriction over a range of Reynolds numbers from 750 to 2000. The study is motivated by the quest to understand the dynamics of flows downstream of severe arterial constrictions. The non-dimensional pulsation frequency is fixed to a value of 0.024 and this, along with the chosen range of Reynolds numbers, gives a parametric range which is relevant to blood flow in the larger arteries of the human cardiovascular system. It is found that despite the relative simplicity of the flow configuration employed here, the flow downstream of the constriction in the current simulations, exhibits a number of features observed before in experiments carried out in more realistic configurations. Examination of the vortex dynamics indicates that the dynamics of the flow downstream of the constriction is dominated by two shear layers, one of which separates from the lip of the constriction and the other, from the lower wall. Flow visualizations show that beyond a Reynolds number of 1000, a series of distinct Kelvin–Helmholtz type vortices are formed in the shear layer that separates off the lip of the constriction. Below this Reynolds number, the formation of these vortices is not readily evident from the flow visualizations. The appearance of these vortex structures at higher Reynolds numbers is in line with previous experiments of Cassanova & Giddens (1978) and Lu *et al.* (1983) which were carried out in axisymmetric configurations.

Mean flow and pressure distribution computed over a number of cycles indicate a relatively large mean recirculation region on the lee side of the constriction, and this region is found to reduce in size with increasing Reynolds number. There is a significant drop in the pressure across the constriction for all the Reynolds numbers simulated here, and this is attributed to increased mixing induced by the shear layers downstream of the constriction. As expected, the mean recirculation zones are associated with low values of skin friction, which is well known in the haemodynamics field (Zarins & Glagov 1994).

In order to characterize the dynamics of the complex unsteady flow downstream of the constriction, flow variables have been decomposed into a phase average and a fluctuation from this average. The phase average includes the time-mean as well as the low-frequency portion of the variation which is associated directly with the flow pulsation. On the other hand, the fluctuation from the phase average contains only the high-frequency content which is characteristic of the non-deterministic turbulence associated variations in the flow. The computed turbulent kinetic energy indicates that the two shear layers are the primary turbulence-producing mechanisms in the flow downstream of the constriction. As the Reynolds number increases, the vortex structures that form in these shear layers become more energetic, leading to an increase in the turbulent kinetic energy. However, the increased level of turbulence intensity is accompanied by increased dissipation. This tends to diminish the turbulent kinetic energy faster for the higher-Reynolds-number cases with the net result that by about ten channel heights downstream of the constriction, the magnitude of turbulent kinetic energy is quite similar for all the cases simulated here.

Examination of the wall pressure fluctuations indicates that the highest intensity occurs roughly 3–4 channel heights downstream of the constriction where the separated shear layers impact on the channel walls. This observation is in line with the experimental observations of Tobin & Chang (1976) who found similar behaviour in an axisymmetric configuration. This observation also has relevance to the phenomenon of arterial murmurs, which are sounds attributed to the flow downstream of an arterial constriction. In particular, our simulations support the assertion of Bruns (1959) and Tobin & Chang (1976) that arterial murmurs are most probably caused by the interaction of the shear layers with the arterial wall and not by the pressure fluctuations associated with flow turbulence in the core flow. Owing to the very same phenomena of shear layer–wall interactions, the fluctuation in the wall shear stress is also the highest in this region, and this has implications for the localization of arterial pathologies and atherosclerosis (Zarins & Glagov 1994).

Finally, the spectral characteristics of the flow downstream of the constriction are examined in detail. Over the entire range of Reynolds numbers covered in the current study, the frequency spectra indicate the presence of a characteristic frequency in the upper shear layer. For Reynolds numbers higher than 1000, this frequency has been associated with the formation of distinct Kelvin–Helmholtz type rollers in the shear layer. At lower Reynolds number, the formation of these vortex structures is not readily apparent, and it is hypothesized that the frequency corresponds to an oscillation in the shear layer. This frequency is observed to increase monotonically with Reynolds number and this is consistent with the observations of Jones & Fronek (1987). A fit through the limited data available from the current simulations suggests that the non-dimensional shear-layer vortex-formation frequency increases as $Re^{0.37}$. Similar shear-layer vortex formation has been observed in bluff-body wakes (Sakamoto & Haniu 1990; Prasad & Williamson 1996) and there, too, its frequency has been found to increase monotonically with Reynolds number. Thus, the connection

between poststenotic and bluff-body wakes flows that was postulated by Bruns (1959) turns out to be generally valid. Some limited results on the lower shear-layer spectra are also presented which indicate that this shear layer exhibits the formation of vortices at a characteristic frequency which is somewhat lower than the corresponding frequency of the upper shear layer.

The frequency spectra corresponding to the streamwise velocity indicate that even at the highest Reynolds number of 2000, the flow up to the region where the separated shear layers attach to the channel walls is at most transitional in nature. Downstream of this region, as the shear layer undergoes transition, the vortex structures associated with the shear layers experience complex interactions among themselves and the wall. This finally results in a turbulent flow which exhibits a well-defined inertial subrange, at least for the higher Reynolds numbers. In this turbulent region, the frequency spectra is observed to break from a $-5/3$ to a -7 slope at roughly the frequency corresponding to the shear-layer frequency. Thus, even though the shear layers themselves have disintegrated by the time the flow convects into this region, the dynamics of the turbulent flow is clearly governed by the shear-layer dynamics. At Reynolds number lower than 1000, no inertial subrange is observed, suggesting that in this range, there is never a full transition to turbulence. The velocity frequency spectra at the higher Reynolds numbers also show some indication of an $S^{-10/3}$ scaling in the region upstream of where a well-developed turbulent flow is observed. This provides some support for past experimental studies (Kim & Corcoran 1974; Lu *et al.* 1983) that have reported the presence of such a scaling in flows downstream of constrictions.

The frequency spectra corresponding to the pressure fluctuations have been analysed in detail. In the region occupied by the separated upper shear layer, the pressure spectra also exhibit a clear peak corresponding to the periodic vortex formation. Further downstream, the pressure spectrum indicates a break in slope at roughly the frequency corresponding to the characteristic frequency of the lower shear layer. Furthermore, there are some indications that at the higher Reynolds numbers, the pressure fluctuation spectra in the mid-channel region exhibit a $S^{-11/3}$ scaling which is consistent with the scaling attributed to turbulence-mean-shear interactions by George *et al.* (1984).

Wall pressure fluctuation spectra have also been analysed in regions where the intensity of the pressure fluctuations is high. For the entire range of Reynolds numbers studied here, it is found that the wall pressure spectra exhibits a sharp break in the slope at a frequency corresponding roughly to the shear-layer frequency. This has important implications for the production and analysis of arterial murmurs. If we accept the hypothesis that the arterial murmurs are primarily caused by wall pressure fluctuations (Bruns 1959; Lees & Dewey 1970; Tobin & Chang 1976), then the current simulations suggest that the signature of the shear-layer frequency should clearly be present in the frequency spectrum of the arterial murmurs. Thus, our conclusion is very much in line with Jones & Fronek (1987) who have suggested that acoustic signals from flows through constricted arteries should contain information about the shear-layer frequency. Therefore, a better understanding of this relationship between the wall pressure spectrum and the shear-layer dynamics could potentially lead to more accurate non-invasive acoustic methods for diagnosing the severity of arterial constrictions.

These computations have been performed at the National Center for Supercomputing (NCSA) at the University of Illinois at Urbana-Champaign. Insightful and detailed

comments from one of the reviewers greatly improved the quality of the paper. We would also like to thank Mrs Jodi Gritten-Dorsett for retyping the entire manuscript.

REFERENCES

- AHMED, S. A. & GIDDENS, D. P. 1983 Flow disturbance measurements through a constricted tube at moderate Reynolds numbers. *J. Biomech.* **16**, 955–963.
- AHMED, S. A. & GIDDENS, D. P. 1984 Pulsatile poststenotic flow studies with laser Doppler anemometry. *J. Biomech.* **17**, 695–705.
- ASK, P., HOK, B., LYOD, D. & TERIO, H. 1995 Bio-acoustic signals from stenotic tube flow: state of the art and perspectives for future methodological development. *Med. Biol. Engng Comput.* September, 669–675.
- BATCHELOR, G. K. 1953 *The Theory of Homogeneous Turbulence*. Cambridge University Press.
- BOMBERGER, R. A., ZARINS, C. K. & GLAGOV, S. 1981 Subcritical arterial stenosis enhances distal atherosclerosis. *J. Surg. Res.* **30**, 205–212.
- BROWN, G. L. & ROSHKO, A. 1974 On density effects and large structure in turbulent mixing layers. *J. Fluid Mech.* **64**, 775–796.
- BRUNS, D. L. 1959 A general theory of the causes of murmurs in the cardiovascular system. *Am. J. Med.* September, 360–374.
- CASSANOVA, R. & GIDDENS, D. P. 1978 Disorder distal to modelled stenoses in steady and pulsatile flow. *J. Biomech.* **11**, 441–453.
- CHANDRA, R., DAGUM, L., KOHR, D., MAYDAN, D., McDONALD, J. & MENON, R. 2000 *Parallel Programming in OpenMP*. Morgan Kaufmann.
- CHOI, H., MOIN, P. & KIM, J. 1992 Turbulent drag reduction: studies of feedback control and flow over riblets. *Rep. No. TF-55*, Thermosci. Div. Dept of Mech. Engng, Stanford University.
- CHORIN, A. J. 1968 Numerical solution of the Navier–Stokes equations. *Math. Comput.* **22**, 745–757.
- CLARK, C. 1976a The fluid mechanics of aortic stenosis – I. Theory and steady flow experiments. *J. Biomech.* **9**, 521–528.
- CLARK, C. 1976b The fluid mechanics of aortic stenosis – II. Unsteady flow experiments. *J. Biomech.* **9**, 567–573.
- CLARK, C. 1977 Turbulent wall pressure measurements in a model of aortic stenosis. *J. Biomech.* **10**, 461–472.
- CREECH JR, O. 1957 A surgeon's view of atherosclerosis. *Am. Heart J.* **54**, 641.
- DUNCAN, G. W., GRUBER, J. O., DEWEY, C. F., MEYERS, G. S. & LEES, R. S. 1975 Evaluation of carotid stenosis by phonoangiography. *New Engl. J. Med.* **293**, 1124–1128.
- ETKIN, B., KORBACHER, G. K. & KEEFE, R. T. 1957 Acoustic radiation from a stationary cylinder in a fluid stream (aeolian tones). *J. Acoust. Soc. Am.* **29**.
- FERZIGER, J. H. & PERIC, M. 1999 *Computational Methods for Fluid Dynamics*. Springer.
- FREDBERG, J. J. 1977 Origin and character of vascular murmurs: model studies. *J. Acoust. Soc. Am.* **61**, 1077–1085.
- FRIEDMAN, M. H., HUTCHINS, G. M., BARGERON, C. B., DETERS, O. J. & MARK, F. F. 1981 Correlation between intimal thickness and fluid shear in human arteries. *Atherosclerosis* **39**, 425–436.
- FUNG, Y. C. 1997 *Biomechanics: Circulation*, 2nd edn. Springer.
- GEORGE, W. K., BEUTHER, P. D. & ARNDT, R. E. A. 1984 Pressure spectra in turbulent free shear flows. *J. Fluid Mech.* **148**, 155–191.
- GERMANO, M., PIOMELLI, U., MOIN, P. & CABOT, W. 1991 A dynamic subgrid-scale eddy viscosity model. *Phys. Fluids A* **3**, 1760–1765.
- GIDDENS, D. P., MABON, R. F. & CASSANOVA, R. A. 1976 Measurements of disordered flow distal to subtotal vascular stenoses in the thoracic aortas of dogs. *Circ. Res.* **89**, 112–119.
- GIDDENS, D. P., ZARINS, C. K. & GLAGOV, S. 1993 The role of fluid mechanics in the localization and detection of atherosclerosis. *J. Biomech. Engng* **115**, 588–594.
- HINZE, J. O. 1975 *Turbulence*. McGraw-Hill.
- INOUE, E. 1954 The application of turbulence theory to oceanography. *J. Met. Soc. Japan* **28**, 441–456.
- JONES, S. A. & FRONEK, A. 1987 Analysis of break frequencies downstream of a constriction in a cylindrical tube. *J. Biomech.* **20**, 319–327.

- KALTENBACH, H.-J., FATICA, M., MITTAL, R., LUND, T. S. & MOIN, P. 1999 Study of flow in planar asymmetric diffuser using large-eddy simulation. *J. Fluid Mech.* **390**, 151–186.
- KHALIFA, A. M. A. & GIDDENS, D. P. 1978 Analysis of disorder in pulsatile flows with applications to poststenotic blood velocity measurements in dogs. *J. Biomech.* **11**, 129–141.
- KHALIFA, A. M. A. & GIDDENS, D. P. 1981 Characterization and evolution of post-stenotic flow disturbances. *J. Biomech.* **14**, 279–296.
- KIM, B. M. & CORCORAN, W. H. 1974 Experimental measurements of turbulence spectra distal to stenoses. *J. Biomech.* **7**, 335–342.
- KU, D. N. 1997 Blood flow in arteries. *Annu. Rev. Fluid Mech.* **29**, 399–434.
- KU, D. N., GIDDENS, D. P., ZARINS, C. K. & GLAGOV, S. 1985 Pulsatile flow and atherosclerosis in the human carotid bifurcation. *Atherosclerosis* **5**, 293–302.
- LEES, R. S. & DEWEY JR, C. 1970 Phonoangiography: a new noninvasive diagnostic method for studying arterial disease. *Proc. Natl Acad. Sci.* **67**, 935–942.
- LESIEUR, M. & MÉTAIS, O. 1996 New trends in large-eddy simulations of turbulence. *Annu. Rev. Fluid Mech.* **28**, 45–82.
- LIEBER, B. B. & GIDDENS, D. P. 1990 Post-stenotic core flow behaviour in pulsatile flow and its effects on wall shear stress. *J. Biomech.* **23**, 597–605.
- LIGHTHILL, J. 1975 *Mathematical Biofluidynamics*. SIAM, Philadelphia.
- LILLY, D. K. 1992 A proposed modification of the Germano subgrid scale closure method. *Phys. Fluids A* **3**, 2746–2757.
- LOUDON, C. & TORDESILLAS, A. 1998 The use of the dimensionless Womersley number to characterize the unsteady nature of internal flows. *J. Theor. Biol.* **191**, 63–78.
- LU, P. C., GROSS, D. R. & HWANG, N. H. C. 1980 Intravascular pressure and velocity fluctuations in pulmonic arterial stenosis. *J. Biomech.* **13**, 291–300.
- LU, P. C., HUI, C. N. & HWANG, N. H. C. 1983 A model investigation of the velocity and pressure spectra in vascular murmurs. *J. Biomech.* **16**, 923–931.
- McKUSICK, V. A. 1958 *Cardiovascular Sounds*. Williams & Wilkins, Baltimore.
- MITTAL, R. & BALACHANDAR, S. 1997 On the inclusion of three-dimensional effects in simulations of two-dimensional bluff-body wake flows. *Proc. 1997 ASME Fluids Engng Div. Summer Meeting, Vancouver, Canada*. FEDSM97-3281.
- MITTAL, R. & MOIN, P. 1997 Suitability of upwind-biased finite difference schemes for large-eddy simulation of turbulent flows. *AIAA J.* **35**, 1415–1417.
- MITTAL, R., SIMMONS, S. P. & UDAYKUMAR, H. S. 2001a Application of large-eddy simulation to the study of pulsatile flow in a modelled arterial stenosis. *J. Biomech. Engng* **123**, 325–332.
- MITTAL, R., VENKATASUBRAMANIAN, S. & NAJJAR, F. M. 2001b Large-eddy simulation of flow through a low-pressure turbine cascade. *AIAA Paper 2001-2560*.
- NEREM, R. M. 1992 Vascular fluid mechanics, the arterial wall and atherosclerosis. *J. Biomech. Engng* **114**, 274–282.
- NICHOLS, W. W. & O'ROURKE, M. F. 1998 *McDonald's Blood Flow in Arteries: Theoretical, Experimental and Clinical Principles*. 4th edn. Oxford University Press.
- ORLANDI, P. 1989 A numerical method for direct simulation of turbulence in complex geometries. *CTR Annual Research Briefs – 1989*, pp. 215–229. Center for Turbulence Research, Stanford University/NASA Ames Research Center.
- PEDLEY, T. J. 1980 *The Fluid Mechanics of Large Blood Vessels*. Cambridge University Press.
- PIOMELLI, U. 1999 Large-eddy simulation: achievements and challenges. *Prog. Aerospace Sci.* **35**, 335–362.
- PITTS, W. H. & DEWEY, C. F. 1979 Spectral and temporal characteristics of post-stenotic turbulent wall pressure fluctuations. *J. Biomech. Engng* **101**, 89–95.
- PRASAD, A. & WILLIAMSON, C. H. K. 1996 The instability of the separated shear layer from a bluff body. *Phys. Fluids* **8**, 1347–1349.
- REYNOLDS, W. C. & HUSSAIN, A. K. M. F. 1972 The mechanics of an organized wave in turbulent shear flow. Part 3. Theoretical models and comparisons with experiments. *J. Fluid Mech.* **54**, 263–288.
- ROACH, M. R. 1963 Change in arterial distensibility as a cause of poststenotic dilatation. *Am. J. Cardiol.* **12**, 802–815.
- ROGALLO, R. S. 1981 Numerical experiments in homogeneous turbulence. *NASA TM 81315*, NASA Ames Research Center, Moffett Field, CA 94035.

- ROGALLO, R. S. & MOIN, P. 1984 Numerical simulation of turbulent flows. *Annu. Rev. Fluid Mech.* **16**, 99–137.
- ROSENFELD, M., KWAK, D. & VINOKUR, M. 1991 A fractional step solution method for the unsteady incompressible Navier–Stokes equations in generalized coordinate systems. *J. Comput. Phys.* **94**, 102–137.
- SAKAMOTO, H. & HANIU, H. 1990 A study of vortex shedding from spheres in a uniform flow. *J. Fluids Engng* **112**, 386–392.
- SCOTTI, A. & PIOMELLI, U. 2001 Turbulent models in pulsating flows *AIAA Paper* 2001-0729.
- SIMMONS, S. P. 2001 Numerical study of pulsatile flow in a modelled arterial stenosis. MS Thesis, Dept Mech Engng, University of Florida, Gainesville, Florida, USA.
- SPALART, P. R., MOSER, R. D. & ROGERS, M. M. 1991 Spectral methods for the Navier–Stokes equations with one infinite and two periodic directions. *J. Comput. Phys.* **96**, 297–324.
- STEIN, P. D., WALBURN, F. J. & SABBABH, H. N. 1982 Turbulent stresses in the region of aortic and pulmonary valves. *J. Biomech. Engng* **104**, 238–244.
- STRANDNESS JR, D. E. 1994 Non-invasive assessment of vascular disease. *Textbook of Cardiovascular Medicine* (ed. E. J. Topol) pp. 2541–2562. Lippincott-Raven, Philadelphia.
- TAYLOR, T. W. & YAMAGUCHI, T. 1994 Three-dimensional simulation of blood flow in an abdominal aortic aneurysm—steady and unsteady flow cases. *J. Biomech. Engng* **116**, 89–97.
- TENNEKES, H. & LUMLEY, J. L. 1972 *A First Course In Turbulence*. MIT Press.
- TOBIN, R. J. & CHANG, I.-D. 1976 Wall pressure spectra scaling downstream of stenoses in steady tube flow. *J. Biomech.* **9**, 633–640.
- TU, C., DEVILLE, M., DHEUR, L. & VANDERSCHUREN, L. 1992 Finite element simulation of pulsatile flow through arterial stenosis. *J. Biomech.* **25**, 1141–1152.
- TU, C. & DEVILLE, M. 1996 Pulsatile flow of non-Newtonian fluids through arterial stenoses. *J. Biomech.* **29**, 899–908.
- TUTTY, O. R. 1992 Pulsatile flow in a constricted channel. *J. Biomech. Engng* **114**, 50–54.
- UCHIDA, S. 1956 The pulsating viscous flow superimposed on the steady laminar motion of incompressible flow in a circular pipe. *Z. Angew. Math. Phys.* **7**, 377–386.
- WILCOX, D. C. 1998 *Turbulence Modelling for CFD*. DCW Industries.
- WINTER, D. C. & NEREM, R. M. 1984 Turbulence in pulsatile flows. *Ann. Biomed. Engng* **12**, 357–369.
- YOUNG, D. F. 1979 Fluid mechanics of arterial stenoses. *J. Biomech. Engng* **101**, 157–175.
- YOUNG, D. F. & TSAI, F. Y. 1979a Flow characteristics in models of arterial stenoses – I steady flow. *J. Biomech. Engng* **6**, 395–410.
- YOUNG, D. F. & TSAI, F. Y. 1979b Flow characteristics in models of arterial stenoses – II unsteady flow. *J. Biomech. Engng* **6**, 547–559.
- ZARINS, C. K. & GLAGOV, S. 1994 Pathophysiology of human atherosclerosis. *Vascular Surgery – Principles and Practice*, pp. 21–39. McGraw-Hill.